Towards high-fidelity simulations of coastal submesoscale baroclinic instabilities with MPAS-O (vE3SM3.0.0) Part II: Realistic experiments

Dylan R. Schlichting[1], Katherine M. Smith[1], Mark R. Petersen[1], Robert D. Hetland[2], Kyle E. Hinson[2], and Darren Engwirda[1,3]

[1]Los Alamos National Laboratory, Los Alamos, NM, USA
[2]Pacific Northwest National Laboratory, Richland, WA, USA
[3]Commonwealth Scientific and Industrial Research Organisation, Australia

Correspondence: Dylan R. Schlichting (dschlichting@lanl.gov)

Abstract. River plumes can strongly influence coastal dynamics but are poorly represented in global ocean models due to stringent resolution requirements. Following the idealized simulations presented in a companion paper (Hinson et al., 2026), this study presents submesoscale-permitting realistic simulations using unprecedented regional refinement with MPAS-O. We assess MPAS-O's ability to represent river plume dynamics by comparing with a validated ROMS configuration focused on the Mississippi–Atchafalaya (M-A) plume in the northern Gulf of Mexico (GoM). The variable-resolution mesh spans 1.4 km in the GoM to 100 km in the Pacific and Indian Oceans. We incorporate several improvements to the representation of river forcing in MPAS-O: the pseudo point source treatment of runoff, river temperature prescribed from air temperature, and passive tracers to track freshwater transport. MPAS-O generates vigorous submesoscales in the open GoM, as quantified by probability density functions of surface relative vorticity and divergence. While the model qualitatively captures the M-A plume's seasonal evolution, it does not realistically reproduce the summer submesoscale eddy field on the Texas–Louisiana shelf. A persistent brackish lens associated with reduced vertical mixing forms and is present throughout the M-A plume. We hypothesize that this arises from interacting parameterization and structural design choices within MPAS-O that affect plume stratification and instability growth under realistic forcing, rather than from deficiencies in numerics. Our results demonstrate MPAS-O's potential for simulating submesoscale processes in the open ocean while highlighting challenges in using regional refinement to model coastal dynamics.

1 Introduction

Unstructured global ocean models are increasingly being tested for their ability to represent coastal processes within global simulations (Mathis et al., 2022; Zhang et al., 2023). Variable resolution meshes provide a computationally efficient means of locally resolving kilometer-scale processes while retaining coarser resolution elsewhere (Tang et al., 2023). As resolution increases, these models can begin to resolve submesoscale processes. Characterized by $\mathcal{O}(1)$ Rossby and Richardson numbers and strong lateral density gradients, these processes play an important role in modulating the vertical exchange of heat, salt, and

nutrients in the upper ocean (McWilliams, 2016; Taylor and Thompson, 2023). Previous studies have shown that unstructured global models (e.g., FESOM, ICON) can statistically reproduce key characteristics of open ocean submesoscale processes (Epke et al., 2025; Uchida et al., 2022).

Extending this capability to coastal regions is challenging because coastal processes are strongly shaped by lateral buoyancy forcing, complex coastlines and bathymetry, and interaction with offshore water masses. As a consequence, coastal regions are characterized by complex flow structures, small spatial scales, and highly heterogeneous mixing. River plumes provide an important example that we will focus on in this study: strong lateral buoyancy gradients associated with river discharge generate submesoscale variability that can regulate exchange between the coastal and open oceans (Lévy et al., 2018; Roobaert et al., 2019; Smith et al., 2016). Accurately representing these processes is therefore important not only for coastal circulation but also for global biogeochemical applications because many global models do not resolve the shelf-scale processes that regulate cross-shelf exchange (Mathis et al., 2022).

In Hinson et al. (2026) (hereinafter Part I), we evaluated the Model for Prediction Across Scales–Ocean (MPAS-O; Ringler et al. 2013) in its representation of coastal submesoscale baroclinic instabilities using idealized simulations of the Mississippi–Atchafalaya (M-A) River plume as an initial test case. We compared MPAS-O against the Regional Ocean Modeling System (ROMS; Shchepetkin and McWilliams 2005) across a range of horizontal resolutions to assess how numerical formulation and subgrid-scale parameterizations influence submesoscale dynamics — an aspect not previously addressed for MPAS-O. We found that at kilometer-scale resolutions, horizontal resolution exerted a stronger control on the simulated dynamics than model choice, indicating that MPAS-O maintains high numerical fidelity in representing coastal submesoscale processes. Here, we extend this assessment to realistic simulations.

The primary objectives of this study are to (1) test whether regional refinement of a global ocean model can produce a dynamically credible representation of realistic coastal submesoscale processes and (2) identify the limitations that emerge as increasingly fine scales are resolved. The study site selected for this investigation of coastal buoyancy-driven flow is the Texas–Louisiana (TXLA) shelf. On the inner shelf (inshore of 50 m depth), seasonal circulation is modulated by regional winds (Zhang et al., 2012a, 2014). On the outer shelf (50-100 m depth), interactions with Loop Current eddies can play an important role (Zhang et al., 2012a, 2014). During summer (JJA), a weak, upcoast diurnal land–sea breeze in near-resonance with the regional inertial period causes freshwater from the M–A rivers to accumulate on the shelf, forming a surface-advected plume. An anisoptropic submesoscale eddy field forms with characteristic diameters of 20-50 km and an associated minimum deformation radius of $\mathcal{O}$(5 km). The resulting summer circulation and stratification have also been extensively studied for their role in modulating seasonal hypoxia (Bianchi et al., 2010). During the non-summer months, downcoast winds narrow the plume and shift it toward a bottom-advected, frictionally influenced state, too constricted to support the large eddies characteristic of summer (Hetland, 2017; Kobashi and Hetland, 2020; Zhang et al., 2014). Submesoscale variability during this period is instead thought to be dominated by relatively unorganized fronts, filaments, and vortices (Kobashi and Hetland, 2020). Although the dominant non-summer submesoscale features remain less understood, the predictable seasonal transition in plume structure and variability makes the TXLA shelf a natural testbed for a global model's ability to capture the seasonal evolution of coastal submesoscale processes.

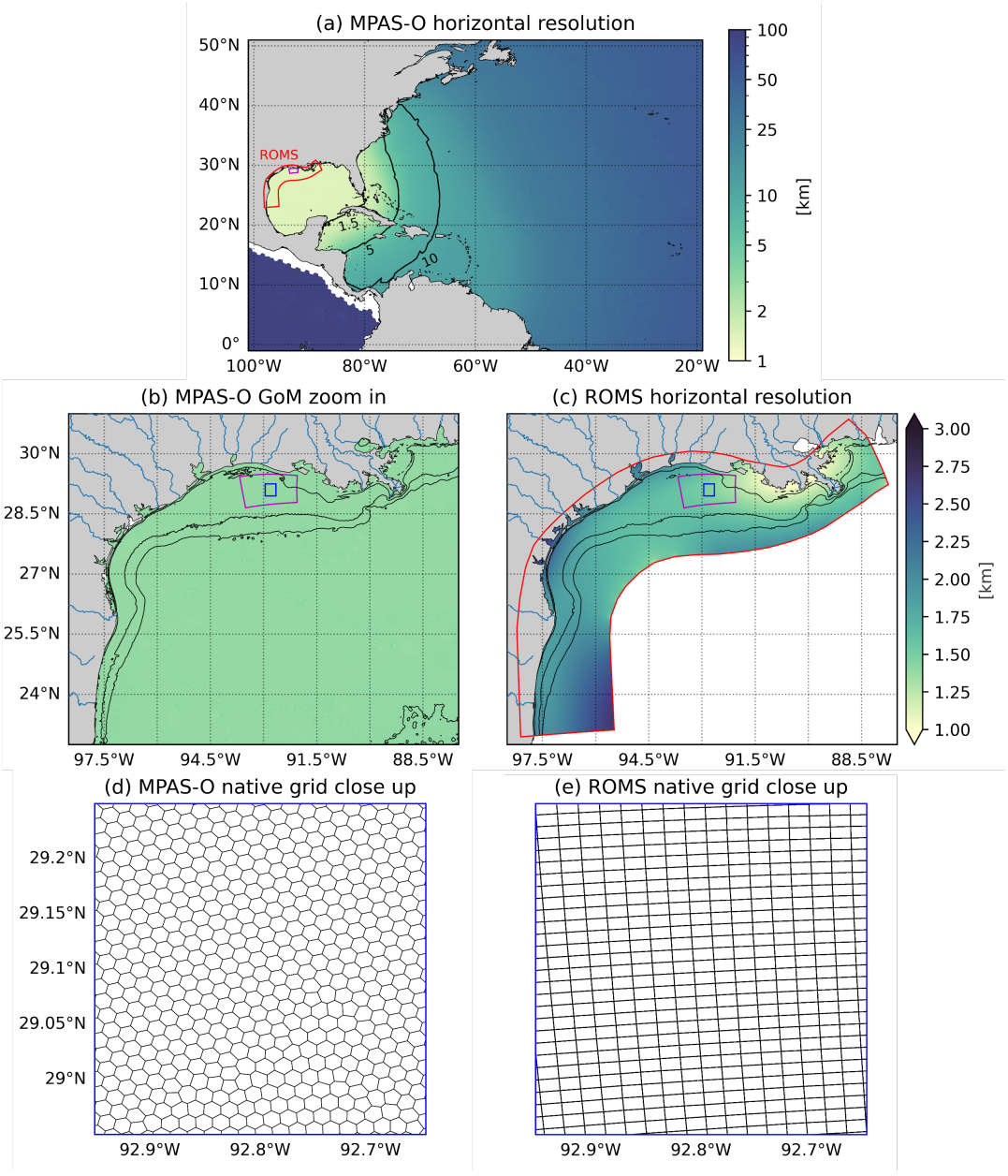


Figure 1. MPAS-O and ROMS horizontal meshes. (a) MPAS-O horizontal resolution, with the 1.5, 5, and 10 km contours marked in black. (b) MPAS-O zoom in the northern Gulf of Mexico, with the 10, 50, and 100 m isobaths marked in black. (c) ROMS model domain and horizontal resolution. The purple box marks the region on the inner shelf used for later statistical analysis. The blue box highlights a close up of the individual cells for (d) MPAS-O and (e) ROMS.

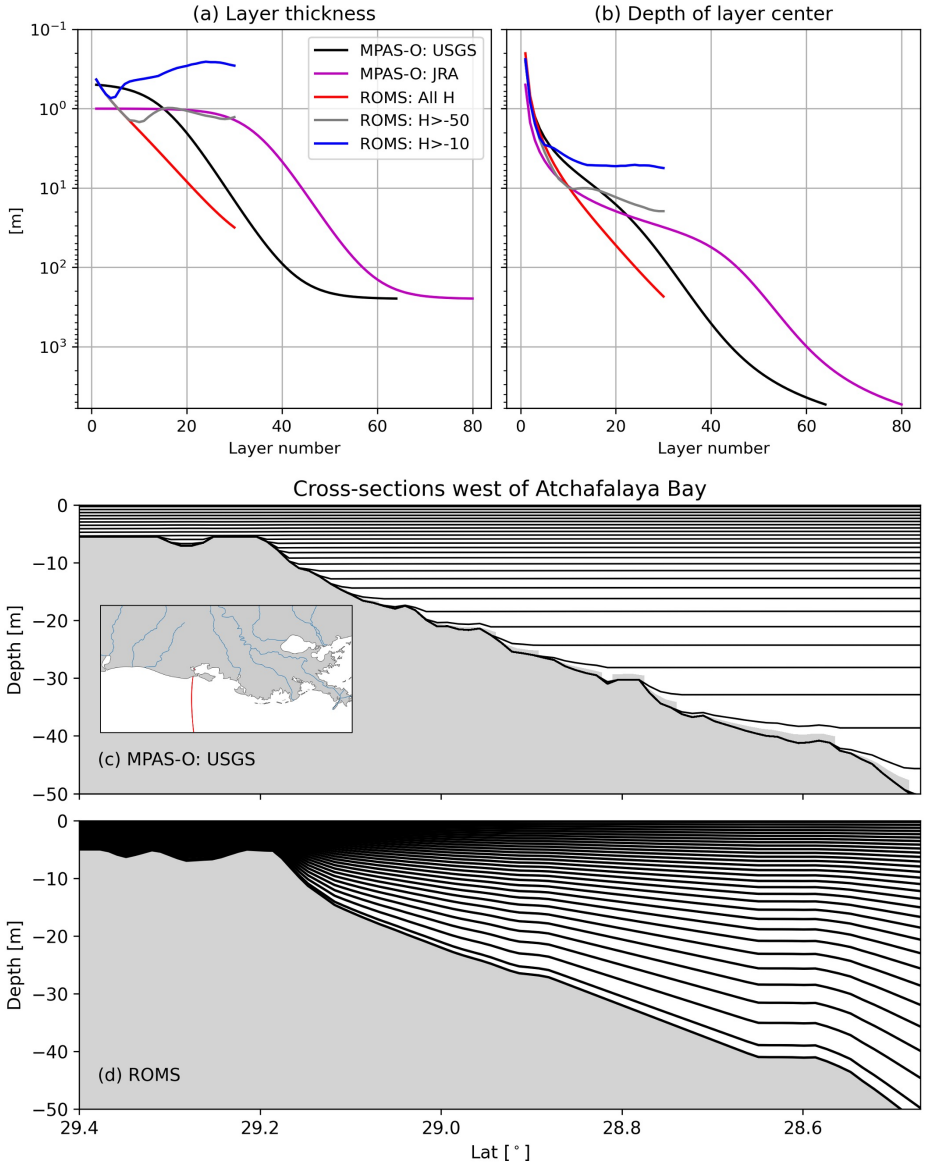


Figure 2. Vertical meshes for MPAS-O and ROMS. (a) Layer thickness, (b) depth of layer center, and sample cross-sections of vertical levels for (c) MPAS-O and (d) ROMS. The red, gray, and blue lines highlight spatial averages of ROMS layer thickness and mid-layer depth for the whole domain, and where the bottom depth H is greater than -50- and -10-m, respectively. The cross-section location is inset in (c).

We present two submesoscale-permitting, regionally-refined MPAS-O simulations of the Gulf of Mexico (GoM) that transition to non-mesoscale-eddying for much of the global domain (Fig. 1a–b). The simulations use unprecedented horizontal (1.4 km) and vertical (0.5-1.0 m, Fig. 2) resolutions for MPAS-O in a realistic configuration within the study region. We compare them against a validated ROMS model (mean resolution 1.7 km) that has been used extensively to study this region. Both

models can be considered submesoscale eddy-resolving with respect to the larger-scale baroclinic instabilities of the summer plume, but increasingly submesoscale-permitting during non-summer months. Smaller-scale processes observed in the region (Körner et al., 2026), such as symmetric and gravitational instabilities, are not resolved by either model.

Earlier iterations of the ROMS model focused on skill assessment and characterization of the larger-scale shelf circulation (Hetland and DiMarco, 2012; Zhang et al., 2012a, 2014), while more recent work has emphasized submesoscale processes (Kobashi and Hetland, 2020; Qu et al., 2022). The model statistically reproduces key characteristics of the summer eddy field, including the eddy kinetic energy and salinity gradient magnitude, with unbiased errors (Kobashi and Hetland, 2020). A two-way nested configuration resolves submesoscale frontal dynamics and has demonstrated skill in reproducing observed processes such as inertially modulated slantwise vertical exchange (Qu et al., 2021, 2022; Schlichting et al., 2023). Given this demonstrated capability, the ROMS setup serves as a robust, process-resolving reference for evaluating MPAS-O simulations on the TXLA shelf.

After detailing the model setup, we first provide a preliminary evaluation of MPAS-O's representation of submesoscale processes in the open GoM, followed by a detailed assessment on the TXLA shelf — including the model's ability to represent both submesoscale variability and the larger-scale seasonal circulation of the M–A plume. As we will show, increasing grid resolution alone is not sufficient to produce a high-fidelity representation of coastal processes within global models. The analyses that follow therefore assess both the dynamical fidelity of the MPAS-O simulations and the practical limitations of regional refinement for representing coastal submesoscale processes in global ocean models.

2 Model setup

A detailed description of the MPAS-O and ROMS solution techniques are provided in Part I. The time-stepping, momentum advection, and tracer advection schemes are unchanged from Part I and are summarized in Table 1 for convenience. One key difference in the present simulations is that the online diagnostics used in Part I to quantify physical and numerical tracer mixing following Burchard and Rennau (2008) are disabled. These diagnostics increase computational run time by 50–85% depending on domain decomposition and are not required to achieve the objectives of this study.

2.1 ROMS

ROMS is configured as part of the Coupled-Ocean-Atmosphere-Wave-Sediment Transport Model (COAWST v3.8, Shchepetkin and McWilliams, 2005; Warner et al., 2005) implementation. Several versions of this model have been used to study processes on the TXLA shelf (Kobashi and Hetland, 2020; Schlichting et al., 2023, 2024; Zhang et al., 2014). The domain covers the TXLA shelf and outer continental slopes (Fig. 1c). The curvilinear mesh has 1.28×10^5 horizontal cells with a mean resolution of 1.7 km; a finer horizontal resolution of 650 m at the M-A River mouths, expanding out to 3.7 km on the outer continental slopes. The model uses 30 terrain-following vertical layers refined at the surface (Fig. 2). The vertical resolution ranges from $\mathcal{O}$(20 cm) close to the coast to $\mathcal{O}$(100 m) near the seafloor on the continental slope. Mean vertical resolutions for

Table 1. Summary of ROMS and MPAS-O model setup. Differences in intra-model setup are denoted with a comma. In the description of lateral boundary conditions, N, S, E, and W refer to north, south, east, and west, respectively. Note that closed boundaries refer to free-slip conditions for the 2D and 3D velocities, no-gradient conditions for tracers, and no-gradient for the free-surface.

Parameter	ROMS: $k-\omega$, ROMS: KPP	MPAS-O: JRA, MPAS-O: USGS
Horizontal cells	1.3×10^5	1.3×10^6
Horizontal res. [km]	0.6–3.7	1.4–100
Vertical layers	30	80, 64
Vertical res. [m]	0.1–435	1.0–250, 0.5–250
Momentum advection	Third-order upwind (horz) & Fourth-order centered (vert) (Shchepetkin and McWilliams, 1998)	Second-order centered (Ringler et al., 2010)
Tracer advection	MPDATA (Smolarkiewicz and Margolin, 1998)	Flux corrected transport (Skamarock and Gassmann, 2011)
Baroclinic time-stepping	Third-order Adams Bashforth (Shchepetkin and McWilliams, 2009)	Second-order Adams Bashforth (Golaz et al., 2025)
Baroclinic Δt [s]	75	30
Barotropic time-stepping	Leapfrog third-order Adams-Moulton with forward-backward feedback	Second-order forward backward (Higdon, 2005)
Barotropic Δt [s]	1.9	1.5
Tracer time-stepping	Second-order leapfrog with trapezoidal corrector	First-order forward Euler
Vertical mixing	$k-\omega$ & Native KPP	CVMix KPP
Background ν_v [$\mathrm{m^2 s^{-1}}$]	10^{-5}, 10^{-4}	10^{-4}
Background κ_v [$\mathrm{m^2 s^{-1}}$]	10^{-6}, 10^{-5}	10^{-5}, 0
ν_4^u [$\mathrm{m^4 s^{-1}}$]	None	3×10^7 to 1.0×10^{13}, 2.0×10^7 to 8.0×10^{12}
ν_2^u [$\mathrm{m^2 s^{-1}}$]	0.9 to 5.0	3.0 to 220, 2 to 110
κ_2 [$\mathrm{m^2 s^{-1}}$]	0.2 to 1.0	None
Bottom stress	Quadratic	Quadratic
Bottom drag coefficient	10^{-3}	10^{-3}
Atmospheric forcing	JRA v1.3 repeat year forcing	JRA v1.3 repeat year forcing
River runoff flux	USGS & USACE	JRA-River, USGS & USACE & JRA-River
River temperature	Stefan and Preud'homme (1993)	JRA 10 m air temperature
2D boundary conditions	All: Closed (N); Free-surface: Chapman-explicit (S,E,W); Momentum: Shchepetkin (S,E,W)	All: Closed (at the coast)
3D boundary conditions	All: Closed (N); Momentum & tracers: Radiation (S,E,W); Turbulent kinetic energy: No-gradient (S,E,W)	All: Closed (at the coast)
Surf. boundary conditions	Virtual salt flux	Kinematic volume flux

the entire domain, inshore of 10 m depth, and inshore of 50 m depth are shown in Fig. 2 (a) to better compare with the MPAS-O simulations. The minimum water depth is 5 m. The model uses a 75 s baroclinic timestep and a 1.5 s barotropic timestep.

The vertical mixing scheme deserves special consideration. To be consistent with the last version of the model used for validation (Kobashi and Hetland, 2020), we use the $k-\omega$ scheme for our "base case" (hereinafter ROMS: $k-\omega$), which solves prognostic equations for turbulent kinetic energy k and specific dissipation rate ω. We also perform a simulation using the ROMS specific implementation of the K-Profile Parameterization (KPP, hereinafter ROMS: KPP), which is closest to the KPP formulation included in the MPAS-Ocean configuration of the Community Vertical Mixing (CVMix) library (Large et al., 1994; Van Roekel et al., 2018). See Part I (Hinson et al., 2026) for a more detailed discussion on the differences between ROMS' native KPP scheme and the CVMix implementation. Background viscosity and diffusivity values for the simulations can be found in Table 1. Other aspects of this simulation are the same as ROMS: $k-\omega$. Lateral mixing is parameterized with harmonic viscosity (ν_2^u=5.0 m^2s^{-1}) and diffusivity coefficients (κ_2=1.0 m^2s^{-1}) scaled to the grid size. Lateral viscosity is rotated along terrain-following layers and lateral diffusion is rotated along geopotential surfaces.

The simulations use repeat year forcing from 2003-2004 (Stewart et al., 2020). This is advantageous because it makes it easier to identify model differences that could be obscured by interannual variability. A downside is that it prevents us from validating the simulations with regional climatologies because the forcing from two calendar years is combined. Japanese Reanalysis (JRA) v1.3 is used to provide the following atmospheric forcings every three hours on a 55 km grid (Stewart et al., 2020): 10 m air temperature, pressure, and winds; specific humidity; downward longwave and shortwave radiation; and precipitation. Outgoing longwave is parameterized using the model sea surface temperature. The model applies a Jerlov water type that transitions from Type III near the river mouths to Type IA near the open boundaries (Jerlov, 1951; Paulson and Simpson, 1977). Outgoing shortwave is parameterized using a constant albedo of 0.06 to be consistent with MPAS-O. ROMS uses a virtual salt flux surface boundary condition. Open boundary and climatology forcing is provided by daily output from Global HYCOM Reanalysis, which uses a horizontal resolution of 1/12° (see Code and Data Availability). The model is initialized on Jan 1 from the HYCOM climatology file. Tides are neglected because they are weak in the GoM (DiMarco and Reid, 1998).

As is common practice in regional models (e.g. GETM, Burchard and Bolding 2002), rivers are configured as point sources (Fig. 3c), using United States Geological Survey (USGS) and United States Army Corps of Engineers (USACE) streamflow data from nine regional rivers (see Code and Data Availability): Mississippi, Atchafalaya, Sabine, Calcaseiu, Trinity, Brazos, San Antonio, Lavaca, and Nueces. The overwhelming majority of the transport comes from the M-A rivers (Zhang et al., 2012b). To represent the complex geometry of river outflow, individual rivers may be represented by multiple localized source cells. The Mississippi River is distributed across 43 grid cells and the Atchafalaya across 8 grid cells to better represent observations, while each of the remaining rivers is represented by a single grid cell. For each river, the runoff flux, runoff direction, vertical distribution, temperature, and salinity are prescribed at a land-sea boundary. Horizontal momentum associated with river inflows is represented by prescribing volume fluxes along with their vertical distribution across river cell faces; ROMS then computes horizontal velocities and accounts for the resulting momentum through flux divergence. Volume fluxes for the M-A rivers are distributed as piecewise functions to resemble observations, with the majority of the discharge in the upper 13

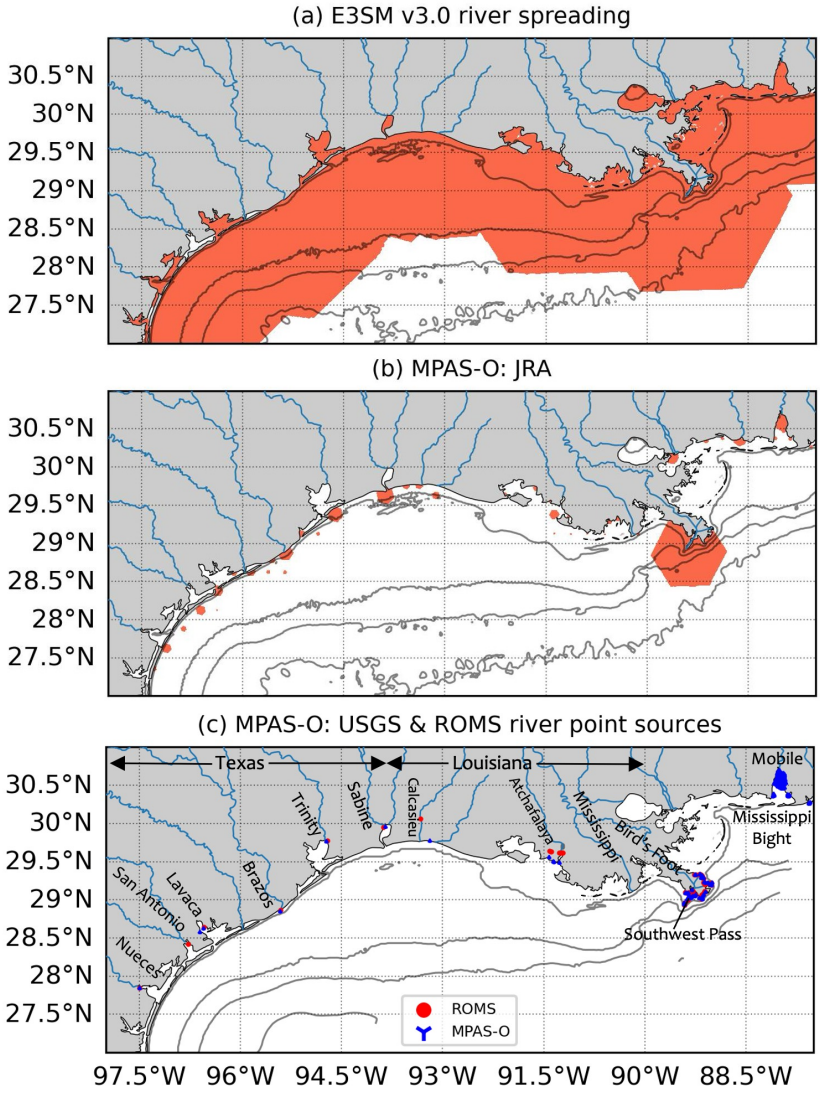


Figure 3. (a) Lateral river spreading in E3SM v3.0 (not used in this study) and (b) MPAS-O: JRA. The red color highlights the lateral spreading of the river volume transport and was saturated for visualization purposes. (c) River point source configuration for ROMS (red dots) and MPAS-O: USGS (blue markers). Other important locations referenced in text are marked in (c). The gray lines are the 10, 50, 100, and 1000 m isobaths, with the MPAS-O isobaths shown in (a-b) and ROMS in (c). Note the Mobile River is included in MPAS-O: USGS but excluded in ROMS.

layers. For the other rivers, volume fluxes linearly decrease over all 30 layers starting from 6.5% in the top vertical layer. The river salinity is set to zero. Daily river temperatures are prescribed using the approach of Stefan and Preud'homme (1993),

where river temperature is estimated from air temperature using the empirical relationship $T_{\text{river}} = 5.0 + 0.75T_a$, where T_a is the air temperature, often collocated with the streamflow gauge.

The spinup time is two years, consistent with previous studies (Große et al., 2019; Hetland, 2017), after which the M-A freshwater volume on the shelf remains relatively constant with respect to the day of year. This is quantified by tagging the M-A rivers with passive dyes similar to Zhang et al. (2012a), who used an earlier version of the ROMS model to study freshwater transport on the shelf. This is discussed more in §3.3. The simulations were run for five years on 120 CPU cores (one node has 128 cores) at the National Energy Research Scientific Computing Center. ROMS: $k-\omega$ achieved approximately 1.9 simulated years per wall-clock day, ROMS: KPP achieved 2.1 simulated years per day. Snapshots and averages of all variables were saved every 12 hours. Analysis of model output was done from years three through five.

2.2 MPAS-O

The simulations use the E3SMv3.0.0 version of MPAS-O (Golaz et al., 2025), only differing in the mesh and a few notable additions to rivers and analysis members described below. The simulations employ MPAS-O coupled to MPAS Sea Ice (Petersen et al., 2019; Turner et al., 2022), forced by data-driven atmosphere and river runoff forcings. The simulations also use the same atmospheric forcing as the ROMS model. MPAS-O uses a kinematic surface boundary condition for volume conservation. The model uses a 30 s baroclinic timestep and a 1.5 s barotropic timestep (Table 1).

The unstructured horizontal mesh is generated using the JIGSAW library (Engwirda, 2017). The mesh has 1.26×10^6 horizontal cells consisting of hexagons and pentagons (Fig. 1d). The target resolution in the GoM is 1.5 km to match the mean resolution of the ROMS model on the inner shelf (Fig. 1e), but the actual resolution is 0.95-1.4 km, with the majority of cells near 1.4 km. The target resolution in the entire GoM is uniform to minimize any potential impacts of flow impedance on Loop Current dynamics. The remainder of the mesh transitions to a target resolution of 60 km in the Atlantic and 100 km in the Pacific and Indian Oceans (not shown) using hyperbolic tangent functions similar to Hoch et al. (2020). Actual resolutions are closer to 55 and 95 km, respectively. The resolution is sub-10 km across part of the North Atlantic and Caribbean Sea (Fig. 1a). We note that high resolution cells in the GoM "leaked" across the Pacific coast of Mexico due to the need to maintain a continuous global ocean and land mesh, as the resolution was unable to discontinuously taper. To prevent numerical instabilities, and because there is sufficient geographical separation from the area of interest, these cells were culled from the ocean mesh.

The simulations use a z^* vertical coordinate with partial bottom cells (Petersen et al., 2015). The layer thickness Δz is calculated as:

$$\Delta z(k) = (\Delta z_{max} - \Delta z_{min}) \tanh \frac{\pi(k - k_0)}{\Delta} + \Delta z_{min}, \tag{1}$$

where k is the layer index, $\Delta z_{max} = 250$ m and Δz_{min} (defined below) are the prescribed maximum and minimum layer thicknesses, respectively, k_0 is the origin in vertical index space of the transition, and $\Delta = 28$ is the number of transition layers over which the $\tanh$ function transitions from Δz_{min} to Δz_{max}. The minimum water depth is 5.0 m.

We show results from two simulations that vary in vertical grid, river forcing, and their horizontal mixing coefficients. The first (MPAS-O: JRA) uses 80 vertical layers with $\Delta z_{min} = 1.0$ m and the second (MPAS-O: USGS) uses 64 layers with

$\Delta z_{min} = 0.5$ m (Fig. 2). MPAS-O: JRA is intended to be more representative of the model run with parameters and forcing used in fully-coupled climate simulations, whereas MPAS-O: USGS was tuned over a number of six month trial simulations to produce the highest-fidelity result with new river forcing. For example, different vertical grids were used because a trial simulation with MPAS-O: USGS that used the same vertical grid as MPAS-O: JRA did not produce submesoscale eddies on the shelf (not shown). Trial simulations of six months were used because the plume, although not spun up, develops sufficient eddies during the first summer for preliminary tuning evaluation. Example cross-sections for MPAS-O: USGS and ROMS near Atchafalaya Bay are shown in Fig. 2 (c-d). We refer the reader to Table 1 for a summary of differences between the MPAS-O simulations.

Vertical mixing is parameterized using KPP as part of the CVMix library (Large et al., 1994; Van Roekel et al., 2018). The model uses harmonic and biharmonic viscosity coefficients scaled to the grid size as:

$$\nu_2^u = \nu_2^0 \left(\frac{\Delta x}{\Delta x_{\text{ref}}} \right), \tag{2}$$

$$\nu_4^u = \nu_4^0 \left(\frac{\Delta x}{\Delta x_{\text{ref}}} \right)^3, \tag{3}$$

where Δx is the cell width, Δx_{ref} is the reference cell width equal to 30 km, and ν_2^0 and ν_4^0 are the background harmonic and biharmonic viscosities, respectively. These coefficients were tuned to be as small as possible without noise appearing at the grid scale such that ν_2^0 is 66.6 m^2s^{-1} for MPAS-O: JRA and 33.3 m^2s^{-1} for MPAS-O: USGS. ν_4^0 is 3.33×10^{11} m^4s^{-1} for MPAS-O: JRA and 2.22×10^{11} m^4s^{-1} for MPAS-O: USGS. No lateral diffusion is applied to the tracers. Mesoscale eddy effects are parameterized at non-eddying resolutions (>20 km) using isoneutral diffusion (Redi, 1982) with a constant, slope-limited diffusivity of 300 m^2 s^{-1} and a Gent–McWilliams scheme (Gent and McWilliams, 1990) with the same constant diffusivity. Both coefficients are linearly tapered to zero between horizontal resolutions of 30 km and 20 km. The Fox-Kemper et al. (2011) scheme, which restratifies the upper ocean through submesoscale mixed layer instabilities, is disabled throughout the domain.

In global models, river runoff fluxes derived from river routing models or observational datasets are often remapped from the terrestrial grid to the ocean grid and spread across many coastal grid cells (Danabasoglu et al., 2020; Golaz et al., 2025). This provides a practical representation of river plume spreading that is otherwise unresolved at coarse resolutions ($\mathcal{O}$(10–100 km)). As resolution approaches the kilometer scale, the prescribed spatial scale of the discharge can substantially exceed the characteristic width of observed plumes and modify the localized buoyancy forcing that drives their resolved dynamics. In response, several global ocean models (e.g., ICON-Coast, ECCO-Darwin) use point source formulations that localize runoff fluxes to one or more model cells (Sun et al., 2017; Mathis et al., 2022; Savelli et al., 2026). However, the common application of a single configuration globally across rivers of widely varying discharge and coastal geometry can still result in point source schemes that are typically less flexible than those used in regional models, which can assign specific characteristics (e.g., salinity, vertical runoff distribution) for individual rivers.

In E3SM v3.0, river runoff fluxes are prescribed daily from the 0.25° JRA river discharge dataset (Suzuki et al., 2018). Runoff is initially assigned to the ocean grid cell nearest to the location specified by the data and then horizontally distributed

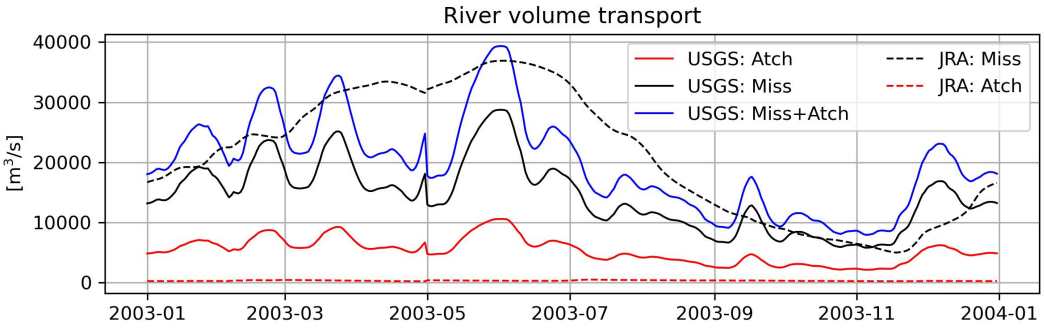


Figure 4. Mississippi and Atchafalaya river volume fluxes calculated from JRA forcing and USGS/USACE streamflow observations. The sharp transition on Apr. 30 is a result of repeat year forcing.

over several surrounding cells using external mapping files (Golaz et al., 2025). The magnitude of the horizontal spreading, which is applied in the same way for each river (i.e., over the same number of grid cells), was originally dictated by Amazon River outflow stability requirements. This resulted in river fluxes being spread hundreds of kilometers offshore (Fig. 3a) and was not tested here. In future E3SM versions, spreading distance will instead scale with each river's inflowing runoff flux (Fig. 3b), using a Gaussian distribution whose length scale depends on both the maximum runoff flux in the JRA forcing and the local grid resolution — allowing the number of grid cells over which runoff is distributed to vary by river according to discharge. For all simulations, the vertical distribution of river runoff follows an exponential decay with depth of the form $\exp(z/0.75)$. The Jerlov water type is set to three everywhere.

In this study, we used this newer spreading in the MPAS-O: JRA simulation to evaluate the model's strengths and limitations when configured in a manner typical of global ocean studies. For example: (1) much of the river water remains spread over the 100 m isobath, where it often exits the shelf permanently (Zhang et al., 2012a, 2014), (2) the spreading distributes Mississippi River water primarily along the western edge of Bird's foot, whereas the ROMS model and observations suggests the rates are closer to 64% (Sorourian et al., 2022), with the remainder distributed around several other passes to the northeast (Fig. 3c), (3) many river discharge points are spuriously placed in the open ocean by the mapping file, and (4) JRA forcing does not account for the USACE's Old River Control structure that diverts roughly 30% of the Mississippi River water to the Atchafalaya (Fig. 4). As a result, the Atchafalaya River volume fluxes are severely underestimated, which contributes to major salinity biases on the shelf (see §3.3).

In the MPAS-O: USGS simulation, we used the same JRA river spreading and forcing as in the MPAS-O: JRA simulation outside of the ROMS model domain. Inside the ROMS domain, the JRA river flux is set to zero and replaced by what we are calling "pseudo point sources" that result in a substantially more realistic river configuration in the nGoM (Fig. 3c). These are the fluxes and locations specified by the USGS streamflow data used in the ROMS simulations interpolated to the nearest MPAS-O grid cell. We refer to them as pseudo point sources because E3SM/MPAS-O has no generic capability to override the mapping file's placement and prescribe river runoff fluxes into specific grid cells. In addition, the horizontal momentum fluxes

associated with the river runoff is still zero and the vertical structure is the same as MPAS-O: JRA, which may significantly alter dynamics in the M-A plume's near-field. There are some small mismatches in the locations of the ROMS point sources and the MPAS-O: USGS pseudo point sources (Atchafalaya, Calcasieu, San Antonio) due to differences in model bathymetry and interpolation discrepancies.

In E3SM v3.0, river runoff temperatures are set equal to the sea surface temperature of the nearest ocean cell. As explicit river temperatures are not yet available from the river model (MOSART), this approach was chosen in the interim in E3SM to preserve energy conservation in fully-coupled simulations. While this nearest-neighbor approach has little impact in coarse-resolution, fully coupled climate simulations, it is problematic in the northern Gulf of Mexico (nGoM), where river temperatures during summer are often cooler than the surrounding ocean. In MPAS-O: JRA trial simulations, this treatment produced spurious temperature spikes at the Mississippi River mouth that could not be corrected by adjusting runtime parameters. To address this, and because energy conservation is not a constraint in the ocean and sea ice only simulations used here, we implemented an option to set river temperatures equal to the 10 m JRA air temperature, with an upper limit of 30°C, keeping river temperatures consistent with observations and ROMS model inputs. This feature is applied to all rivers in both MPAS-O: JRA and USGS simulations. While it substantially improved temperature fidelity in the nGoM relative to the original E3SM v3.0 approach, it likely reduced accuracy in polar regions but is neglected due to the short simulation length. A geographically based hybrid approach will be explored in future work.

The simulations were run on 5120 cores (one node has 128 cores) at Los Alamos National Laboratory Institutional Computing, with 4864 cores used for MPAS-O and 256 cores used for MPAS Sea Ice. MPAS-O: JRA achieved approximately 0.4 simulated years per day and MPAS-O: USGS achieved roughly 0.5 simulated years per day. Snapshots and averages of two dimensional variables were saved every 12 hours, whereas three dimensional variables were saved weekly. MPAS-O: JRA was run for four years to conserve computational resources because it did not produce summer shelf eddies comparable to ROMS throughout the entire simulation (discussed in §3.2). Analysis of model output was conducted over years three through four. MPAS-O: USGS was run for five years and analysis of model output was conducted over years three through five.

3 Results

3.1 Submesoscales in the open GoM

We first assess whether MPAS-O qualitatively reproduces the well-established seasonal cycle of open ocean submesoscale activity. At 1.4 km resolution, the open ocean GoM resolution can be considered submesoscale-permitting, as work by Barkan et al. (2017) showed that the mixed layer deformation radius varies from 1 km in summer to 2.2 km in winter. Fig. 5 shows winter and summer snapshots of relative vorticity normalized by the Coriolis parameter (i.e., the Rossby number), $\zeta f^{-1} = (\partial_x v - \partial_y u)/f$, from the MPAS-O: JRA simulation. Numerous small-scale frontal and filamentary structures with $\mathcal{O}(1)$ Rossby numbers are evident throughout the GoM during winter, including within and around Loop Current eddies, over the continental shelves, and near river outflow regions. These features are less prevalent during summer, consistent with previous studies showing stronger open ocean submesoscale activity in the GoM during winter (Barkan et al., 2017; Bracco et al., 2019;

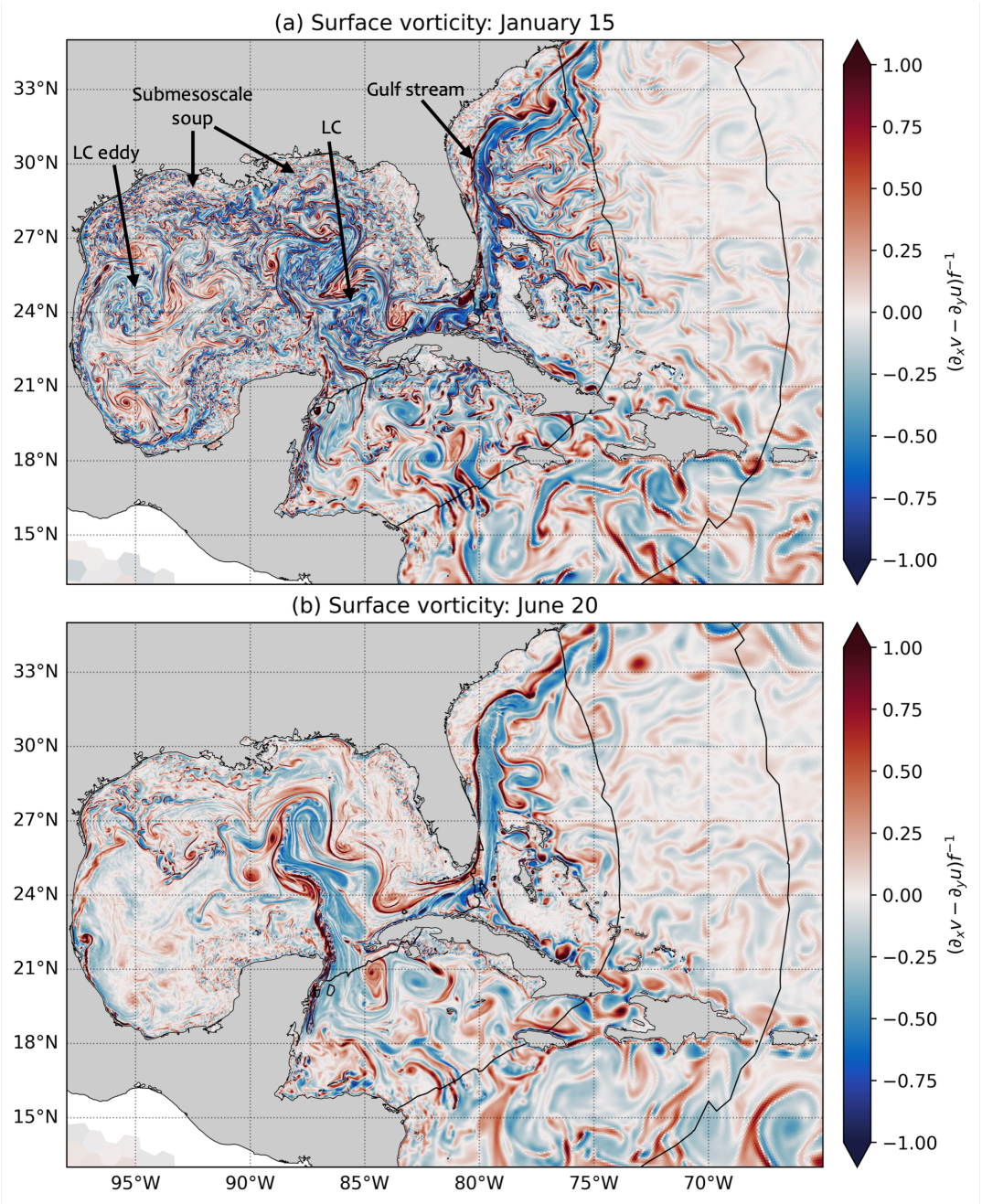


Figure 5. MPAS-O: JRA ζf^{-1} snapshots during (a) winter and (b) summer of year three. The black contours mark 1.5, 5, and 10 km horizontal resolutions. The Loop Current eddy in (a) is confirmed using sea surface height anomalies and is not shown.

Liu et al., 2021; Ntaganou et al., 2024). The seasonal contrast is consistent with the expected enhancement of mixed layer

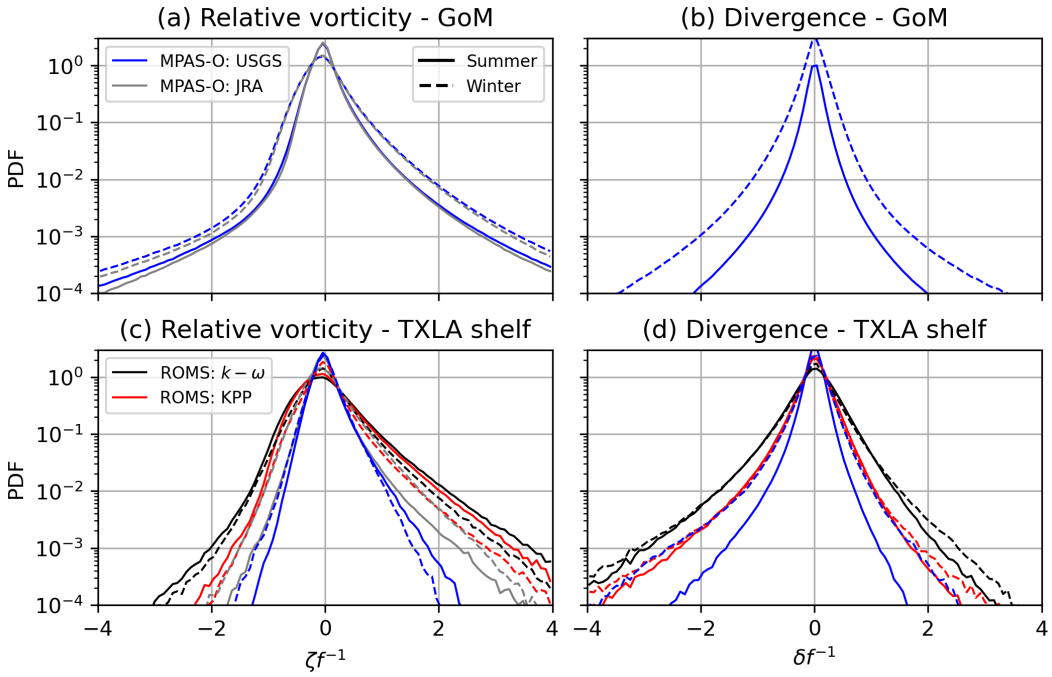


Figure 6. PDFs of (a) ζf^{-1} and (b) δf^{-1} for the MPAS-O simulations inside the entire GoM during summer (JJA, solid lines) and winter (DJF, dashed lines). (c-d) Same as (a-b), but on the TXLA shelf inside the magenta box shown in Fig. 1 for the 4 simulations. Note that δf^{-1} for MPAS-O: JRA (in b,d) is not shown due to a file corruption issue.

instabilities under deeper winter mixed layer conditions (Callies et al., 2015), which increase the amount of available potential energy that can be extracted from lateral density gradients.

Submesoscale variability in the open GoM is also shown with probability density functions (PDFs) of surface normalized relative vorticity (Fig. 6a,c) and divergence $\delta f^{-1} = (\partial_x u + \partial_y v) f^{-1}$ (Fig. 6 b,d). The skewness of these PDFs are hallmarks of abundant submesoscale activity (Balwada et al., 2021; Shcherbina et al., 2013). The relative vorticity PDFs are positively skewed (towards cyclonic vorticity) in both seasons (Fig. 6a), with qualitatively similar distributions among the MPAS-O simulations. The winter distribution exhibits broader tails than the summer distribution. The divergence PDFs are negatively skewed (towards convergence) in both seasons, and likewise exhibit broader tails in winter than in summer. These diagnostics demonstrate the seasonal modulation of submesoscale variability but do not, by themselves, establish the instability mechanisms responsible for generating these features. A detailed analysis of submesoscale generation in the open GoM is beyond the scope of this study, which focuses on the representation of the M-A plume and its associated submesoscale activity.

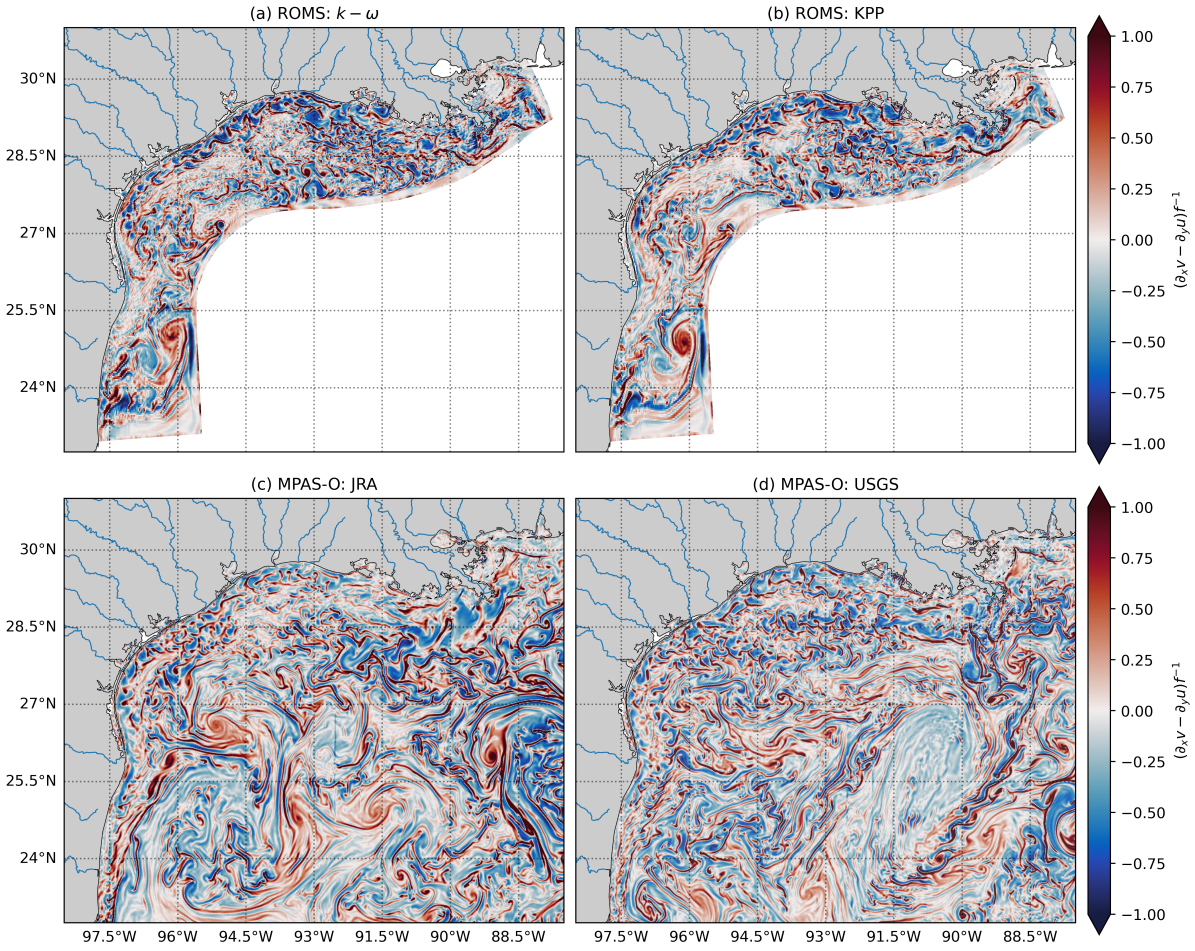


Figure 7. Zoom in of ζf^{-1} snapshots for (a) ROMS: $k-\omega$, (b) and ROMS: KPP, (c) MPAS-O: JRA, and (d) MPAS-O: USGS during winter. Time is the same as Fig. 5 (a).

3.2 Suppression of summer TXLA shelf eddies in MPAS-O

We begin with an analysis of the ROMS simulations because previous studies have shown that the model reproduces the seasonal evolution of the horizontal salinity gradient magnitude and the observed variability in eddy kinetic energy on the TXLA shelf (Kobashi and Hetland, 2020). As discussed in §1, the M-A plume undergoes a dynamical transition between summer conditions, when regional wind patterns cause freshwater to pool on the shelf and broaden the plume, supporting a field of $\mathcal{O}(20\text{–}50)$-km eddies due to the strong lateral salinity gradients that form. During non-summer conditions, mean downcoast winds confine the plume and associated stratification along the shelf, and frequent storms suppress eddies of the same scale from forming (Hetland, 2017; Zhang et al., 2012a, 2014). Instabilities on the shelf are distinct from mixed layer eddies, as eddies extend throughout the water column rather than remaining confined to the mixed layer (Hetland, 2017; Qu

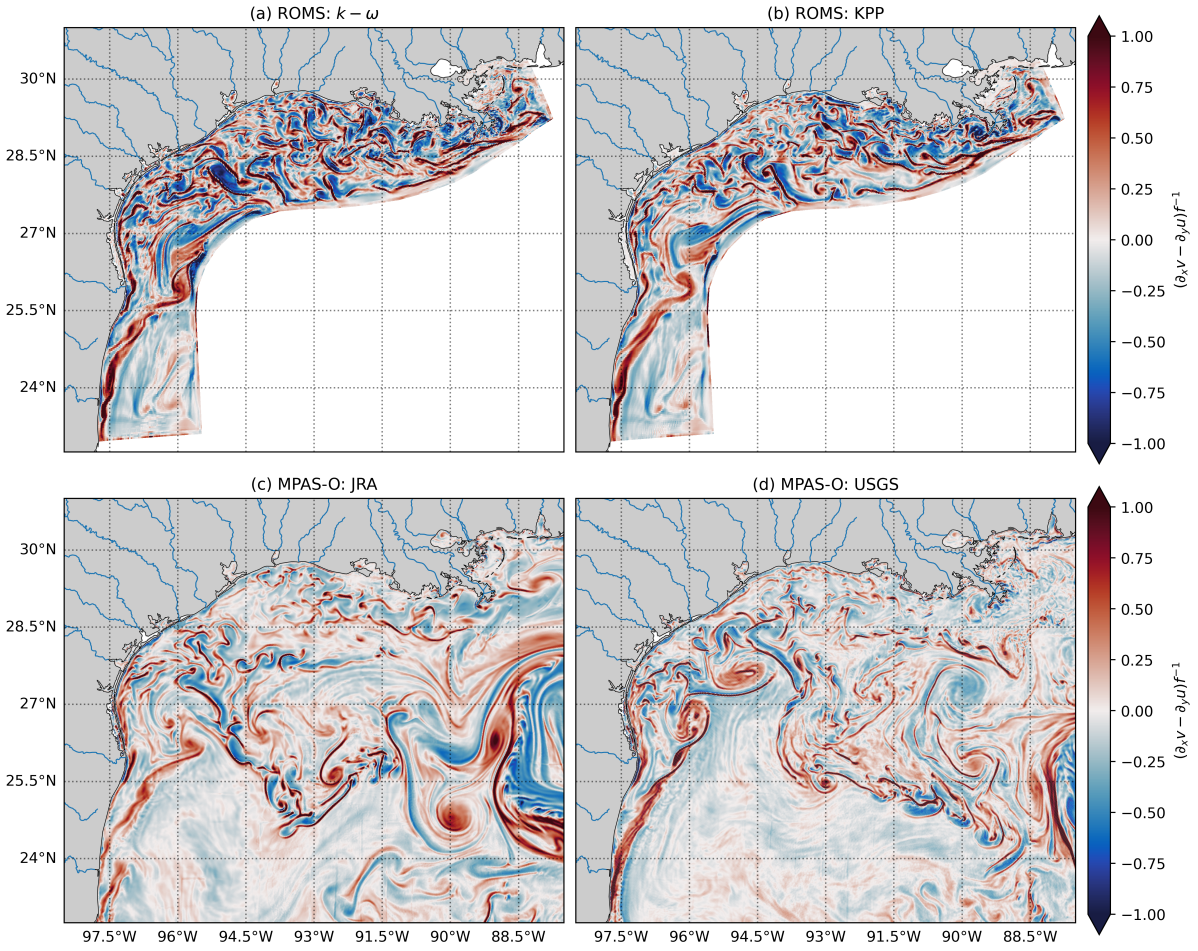


Figure 8. Same as Fig. 7, but for summer. Time is the same as Fig. 5 (b).

et al., 2022). The type of submesoscale processes prominent on the shelf during winter is less understood. We therefore use surface normalized relative vorticity to qualitatively demonstrate the seasonal transition, illustrated by plan view snapshots during winter (Fig. 7a-b) and summer (Fig. 8a-b).

This seasonal variability is further reflected in the normalized relative vorticity and divergence PDFs on the inner shelf. We focus on the inner shelf (0–50 m depth; Fig. 1b–c) because circulation there is primarily wind-driven, whereas outer-shelf variability is more strongly influenced by interaction with Loop Current eddies (Zhang et al., 2012a). Differences between MPAS-O and ROMS on the inner shelf therefore primarily reflect each model's ability to represent the M–A plume, rather than differences in how MPAS-O and HYCOM (used for the ROMS open boundary forcing) represent Loop Current eddies. The normalized relative vorticity distributions narrow slightly during winter (Fig. 6c) — in contrast to the broadening seen in the open-GoM distributions (§3.1) — while the divergence PDFs (Fig. 6d) show the opposite seasonal response, broadening during

winter. To our knowledge, this behavior has not been previously reported. We hypothesize that the broader winter divergence distributions may result from increased wind forcing (Kobashi and Hetland, 2020), which could enhance frontogenesis and produce more intermittent, spatially localized convergence and divergence; this mechanism warrants further investigation but is beyond the scope of this study. ROMS: $k-\omega$ has the broadest distribution of the four simulations for both variables. ROMS: KPP has narrower distributions than ROMS: $k-\omega$. We attribute this to ROMS: KPP being more diffusive. An example of this elevated diffusion is shown in Fig. 9 and discussed below.

A key result is that the MPAS-O simulations (Fig. 8c-d) do not produce a submesoscale eddy field with the same complexity or qualitative characteristics as the ROMS simulations during summer (Fig. 8a-b). We refer to this reduction in submesoscale activity as eddy suppression, meaning a reduction in the growth and persistence of the frontal instabilities. The MPAS-O simulations produce some eddies and organized meanders on the Texas shelf (e.g., west of 93.5°W) but they have weaker relative vorticity than the ROMS model. This is especially true on the Louisiana Shelf for MPAS-O: USGS. Surprisingly, MPAS-O: USGS features less submesoscale activity than MPAS-O: JRA near the M-A river mouths and on the Louisiana shelf despite improved river forcing, increased minimum layer thickness, and reduced horizontal mixing. In contrast, the MPAS-O simulations show substantially better qualitative agreement with ROMS during winter (Fig. 7c-d). Both MPAS-O simulations exhibit numerous small-scale fronts, filaments, and vortices, although these features generally have weaker relative vorticity than those in the ROMS simulations.

These trends are also shown in PDFs of relative vorticity (Fig. 6c), where both MPAS-O simulations have narrower distributions than the ROMS simulations, with MPAS-O: USGS having the smallest distribution for both seasons. Because the characteristic summer eddy field does not form in these simulations, the interpretation of seasonal differences in MPAS-O's PDFs is complicated. For example, MPAS-O: JRA has a broader relative vorticity distribution in winter rather than summer that is nearly identical to ROMS: KPP. On the other hand, MPAS-O: USGS has a larger anticyclonic tail in winter, but is narrower in summer. However, the divergence PDF for MPAS-O: USGS is similar to ROMS: KPP during winter but is substantially weaker in summer than the other simulations.

Fig. 9 shows cross-sections of salinity (a,c,e) and vertical eddy viscosity ν_v (b,d,f) west of Atchafalaya Bay averaged over June of year four, for MPAS-O: USGS and the ROMS simulations. The cross-sections are located in the plume's far-field, defined as the region where the plume has lost all memory of inflowing momentum fluxes (Horner-Devine et al., 2015). The surface boundary layer depth is shown for MPAS-O: USGS (Fig. 9a-b) and ROMS: KPP (Fig. 9c-d) because it is the fundamental diagnostic that controls the extent of nonlocal turbulent mixing. In MPAS-O: USGS, a brackish lens forms in the top several meters of the water column that is absent in the ROMS simulations. The mean boundary layer depth for MPAS-O: USGS is 3.3 m and 3.4 m for ROMS: KPP, but the two may differ by over a meter locally. Values of ν_v are generally smaller in MPAS-O: USGS, except in the ocean interior where the default to prescribed background levels (10^{-5} for ROMS: KPP, 10^{-4} for MPAS-O: USGS). Within the boundary layers, ν_v in ROMS: KPP can exceed MPAS-O: USGS by over an order of magnitude. We note that MPAS-O: USGS demonstrates weaker mixing close to the seafloor relative to ROMS: KPP because CVMix lacks an explicit bottom boundary layer parameterization. In ROMS: KPP, we use a bottom boundary layer parameterization that is analogous to the surface boundary layer parameterization. The salinity and ν_v sections for ROMS: $k-\omega$

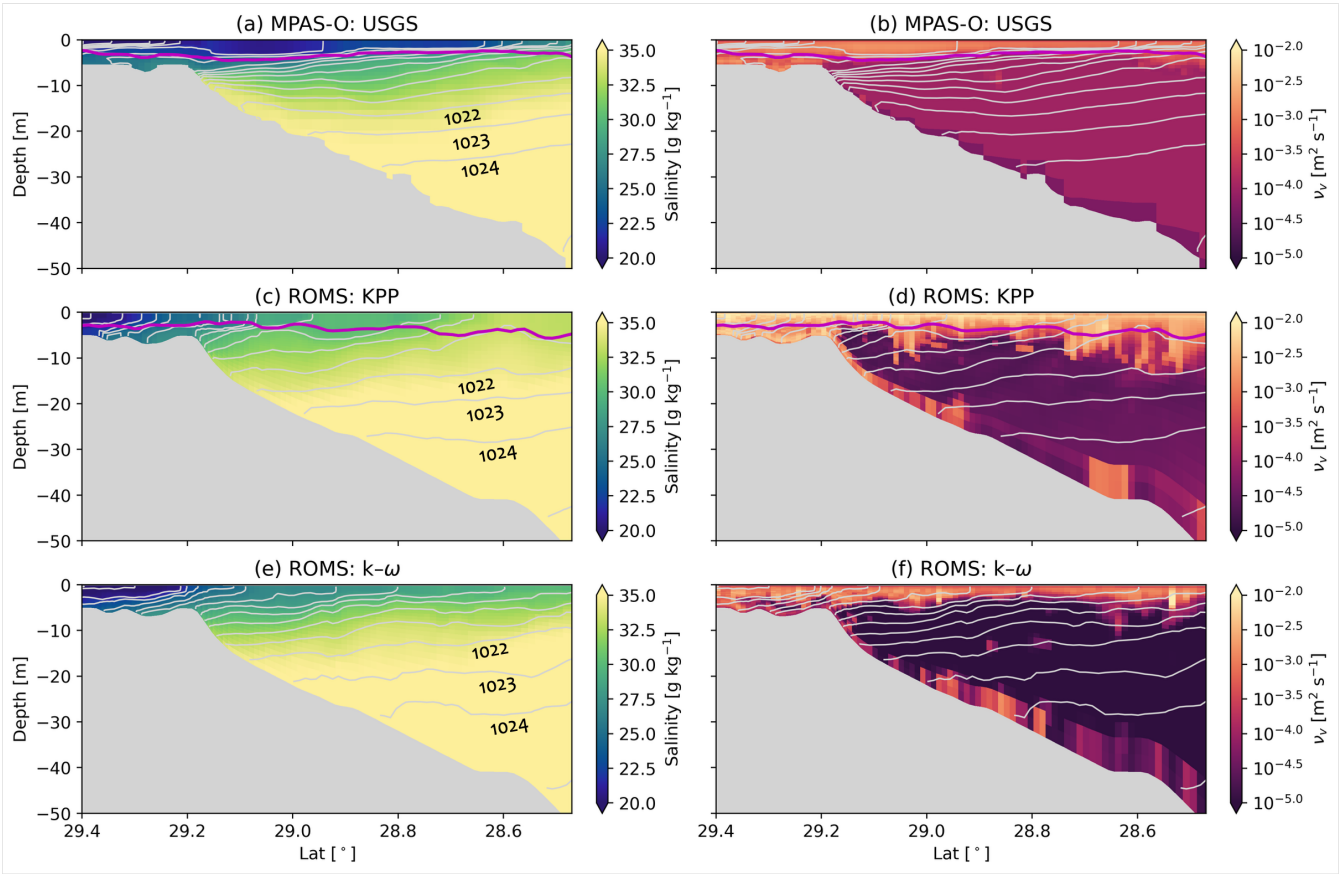


Figure 9. Cross-sections of salinity and vertical eddy viscosity. (a–b) MPAS-O: USGS, averaged over June of year 4, (c–d) ROMS: KPP, and (e–f) ROMS: k–ω. Isopycnals are overlaid in gray at 1 kg m^{-3} intervals and the surface boundary layer depth (calculated online by each models' KPP scheme) is shown with the magenta lines. The cross-section location is the same as in Fig. 2. Note that the boundary layer depth is only available for ROMS: KPP because it is calculated online at every timestep, unlike when $k-\omega$ is used. See McWilliams et al. (2009) for more information.

(Fig. 9e-f) are similar to ROMS: KPP, but ROMS: KPP is generally more diffusive. These trends are also confirmed in PDFs of
315 ν_v computed over the same region as in Fig. 6 (not shown). It remains unclear to what extent the reduced vertical viscosity—and therefore weaker vertical mixing (i.e., destruction of scalar variance)—is a cause of eddy suppression, a consequence of eddy suppression, or how different configuration choices contribute to these behaviors. For example, the CVMix implementation of KPP has not been tuned for coastal buoyancy-driven flows and differs in several respects from ROMS' native KPP scheme (Li et al., 2019). We discuss how various configuration choices could contribute to eddy suppression in MPAS-O in §4.

3.3 MPAS-O's representation of the larger-scale TXLA shelf circulation

The objective of this section is to understand how summer eddy suppression affects MPAS-O's ability to represent the larger-scale circulation and seasonal evolution of the M-A plume. We are also interested in comparing the bulk transport and fate of M-A plume water between models. One tool that accomplishes both simultaneously is an analysis of freshwater dyes following Zhang et al. (2012a), who used an earlier version of the ROMS model to investigate freshwater transport on the TXLA shelf. For all simulations except MPAS-O: JRA, the M-A rivers are tagged using passive dyes ϕ with an initial concentration of one at the point sources and zero elsewhere. A concentration of one means a parcel consists of purely river water, whereas a parcel with a concentration of zero has no river water. We omitted this feature when running MPAS-O: JRA for two reasons: (i) the Atchafalaya River fluxes dramatically differ from streamflow observations (Fig. 4), and (ii) the river spreading scheme for the Mississippi instantaneously deposits freshwater offshore of how the shelf freshwater volume is defined. Thus, we did not expect an analysis of MPAS-O: JRA to be meaningful relative to the other simulations, even if by coincidence the freshwater volume ended up being similar.

We define the freshwater volume V_f for each river as:

$$V_f = \iint\limits_{\Omega_b} \left(\int\limits_{H>-100}^{\eta} \phi(x,y,z,t)\, dz \right) dxdy\,, \tag{4}$$

where Ω_b denotes the lateral boundaries of the ROMS model domain, η is the sea surface height, and ϕ is the dye concentration in each grid cell. We note that the domain volume inshore of the 100 m isobath is approximately 4.4% smaller in ROMS than MPAS-O due to differences in bathymetry and the culling of land cells during the MPAS mesh generation process. Time series of V_f with the river volume fluxes overlaid for the simulations are shown in Fig. 10. After two years, the freshwater volume for both rivers in the ROMS simulations show a clear seasonal cycle with little day of year variability (for the ROMS simulations), confirming the two year spinup time discussed in §2.1.

V_f is strongly correlated with river discharge, with higher discharge corresponding to higher V_f (Zhang et al., 2012a). Previous studies have shown that eddies are the dominant mechanism for transporting material off the shelf (Hetland, 2017; Thyng and Hetland, 2018; Zhang and Hetland, 2018; Zhang et al., 2014), since strong bathymetric gradients at the shelf break otherwise constrain cross-isobath flow and largely isolate shelf and open ocean dynamics. Given that both simulations use the same river discharge within the ROMS domain, we primarily attribute the larger V_f in MPAS-O to reduced submesoscale activity. Differences in Loop Current dynamics may also contribute to differences in freshwater content, since Loop Current eddy interactions influence circulation between the 50–100 m isobaths (Zhang et al., 2012a); in ROMS, Loop Current position is held fixed with respect to day of year through the open boundary forcing, unlike in MPAS-O.

Mississippi River discharge (Fig. 10a) peaks in late March and early June and generally decreases until late November. For the ROMS simulations, V_f is higher in late spring and early summer, peaking in July. Trends are similar for the Atchafalaya (Fig. 10b). For ROMS: $k-\omega$, the maximum correlation between the Mississippi discharge and the freshwater volume is 0.84, which occurs with a 39 day lag (discharge leads volume). The maximum correlation for the Atchafalaya is 0.75, also with a 39 day lag. Results are similar for ROMS: KPP, however the freshwater volume associated with each river are slightly higher

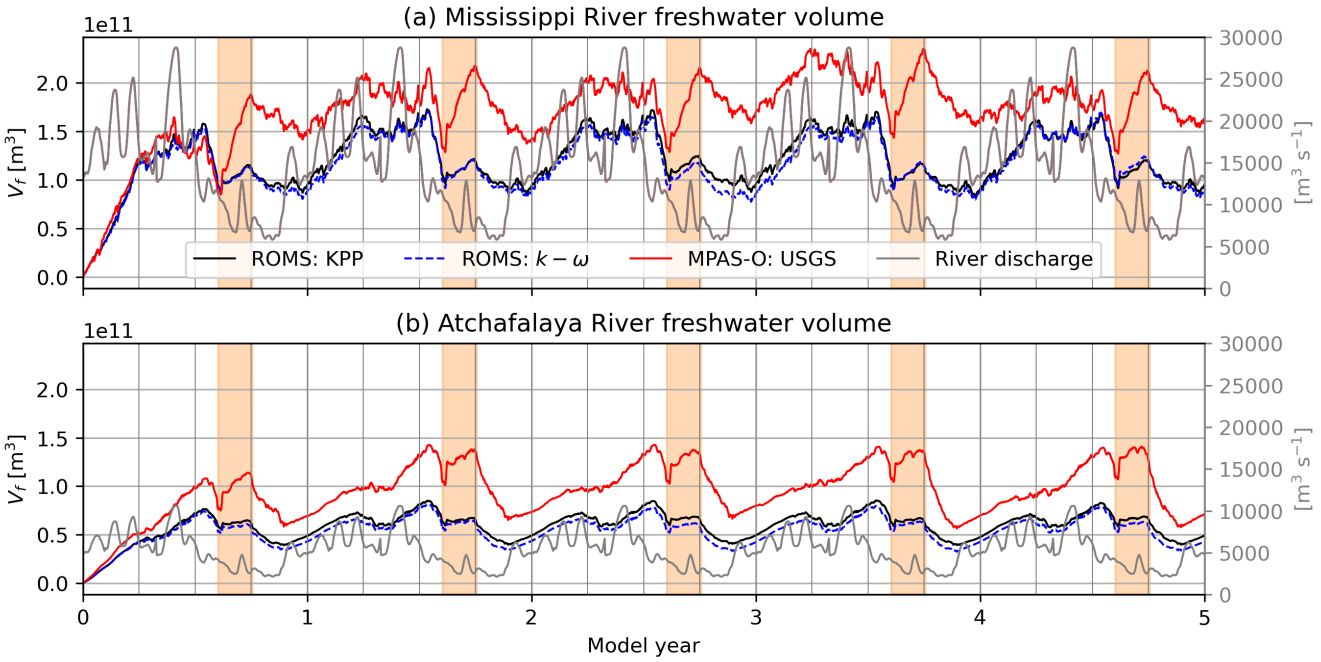


Figure 10. Time series of freshwater volume V_f for the (a) Mississippi and (b) Atchafalaya Rivers. The gray lines show volume fluxes for each river. The shaded orange boxes are from Aug 8 - Oct 3 of each year to highlight significant increases in MPAS-O's freshwater volume that are absent in the ROMS simulations.

than ROMS: $k-\omega$ (4% for the Mississippi, 10% for the Atchafalaya). Thus, it takes over a month for freshwater discharge to interact with the continental shelf before it is possibly exported to open water. We note that Zhang et al. (2012a) performed a similar analysis from 2005-2011 and found similar values for the correlation coefficients, but with lags of 21 days for the Mississippi and 33 days for the Atchafalaya. We attribute this to reduced summer eddy activity for 2003-2004 relative to other years, which can be confirmed by comparing PDFs of surface vorticity (compare Fig. 6 to Fig. 3 of Schlichting et al. 2023).

MPAS-O: USGS qualitatively captures the seasonal evolution of the freshwater volume for both rivers. However, the time-averaged freshwater volume is 42% higher than the ROMS: $k-\omega$ for the Mississippi and 58% higher for the Atchafalaya. In summer, the freshwater volume for MPAS-O: USGS may occasionally be over twice that of the ROMS simulations. The freshwater volume is also more variable year over year in MPAS-O: USGS than the ROMS simulations. This could be due to internal variability in Loop Current dynamics within MPAS-O, whereas Loop Current effects are implicitly represented and held constant from year to year in the open boundary forcing of the ROMS simulations. As a result, correlations between discharge and freshwater volume are lower in MPAS-O: USGS, with a maximum correlation of 0.32 between Mississippi discharge and volume with a 41 day lag. For the Atchafalaya, the maximum correlation is 0.53 with a 56 day lag. This analysis indicates that MPAS-O has much more freshwater on the shelf than ROMS. It also takes longer for freshwater to leave the shelf in MPAS-O, especially for the Atchafalaya.

In addition, there are peaks in MPAS-O: USGS freshwater volume in late summer and early fall that are absent in the ROMS simulations. These peaks occur several weeks after increases in M-A river discharge and intense downcoast winds (not shown). There is a strong northward return flow on the western Texas shelf not present in the ROMS simulations (e.g., 96°W, 23-27°N) and several mesoscale features that appear to be the cause of this excessive freshwater accumulation. This can be interpreted with the help of a supplementary plan view animation of seasonally-averaged M-A freshwater thickness h and transport $\boldsymbol{Q}$ for MPAS-O: USGS and ROMS: $k-\omega$ (see Code and Data Availability), which we define as:

$$h = \int_{-H}^{\eta} \phi \, dz, \tag{5}$$

$$\boldsymbol{Q} = \int_{-H}^{\eta} \boldsymbol{u}_h \, \phi \, dz, \tag{6}$$

where $\boldsymbol{u_h}$ is the horizontal velocity vector.

Plan view plots of seasonally-averaged freshwater thickness and transport (Fig. 11) show that MPAS-O: USGS qualitatively reproduces the extent of the plume and the direction of freshwater transport. Consistent with the freshwater volume, both freshwater thickness and transport may be several times larger in MPAS-O than ROMS: $k-\omega$ locally. For both models, the plume is confined closer to the coast and extends southward toward the Mexico border in winter (Fig. 11a-b). In summer (Fig. 11c-d), the plume shifts northward and spreads over the shelf. Both models contain several similar features on the inner shelf, including (i) a recirculating bulge west of Bird's Foot, which has been extensively documented (Wiseman et al., 1997; Hetland, 2017), (ii) a persistent gyre near 94°W in summer, which is also visible in surface snapshots of relative vorticity (Fig. 8b), and (iii) the largest freshwater transport generally occurs near the M-A river mouths, consistent with Zhang et al. (2012a). The freshwater thickness is larger in MPAS-O: USGS than the ROMS simulations on most of the shelf.

On the continental slopes (see red lines in Fig. 11), model differences are more dramatic and highlight a limitation of using a limited-domain model. In ROMS, the freshwater thickness and transport is smaller year round. This is likely due to the radiation boundary conditions and the climatological nudging layer, which relaxes the passive dyes to zero over the first 10 interior grid points. Thus, we do not expect the behavior of the ROMS model to be realistic close to the open boundaries. Despite the lack of shelf eddies, a major advantage of MPAS-O is that it can be used to study the fate and transport of M-A river water into the open GoM. For example, the imprint of M-A river water is apparent as far south as 22°N and on the Florida shelf, interacting with the Loop Current and numerous mesoscale features. It can also be seen in the Gulf Stream (not shown). An interesting result is that the freshwater transport in the Loop Current eddies can exceed the transport on much of the shelf, likely due to the energetic surface currents.

Finally, we compare the surface tracer fields between the simulations using summer (Fig. 12) and winter (Fig. 13) averages of sea surface salinity (SSS) and temperature (SST). The 33 g kg^{-1} isohaline, which is the operational plume boundary (Hetland and Hsu, 2013; Kobashi and Hetland, 2020), and the 100 m isobath, are shown in the SSS panels (Figs. 12-13a-d). These complement the freshwater analysis by highlighting the seasonal variability of the plume extent in a different way. Differences between ROMS: $k-\omega$ SSS and the MPAS-O simulations (ΔSSS) are shown in Figs. 12- 13 e-f with MPAS-O fields interpolated

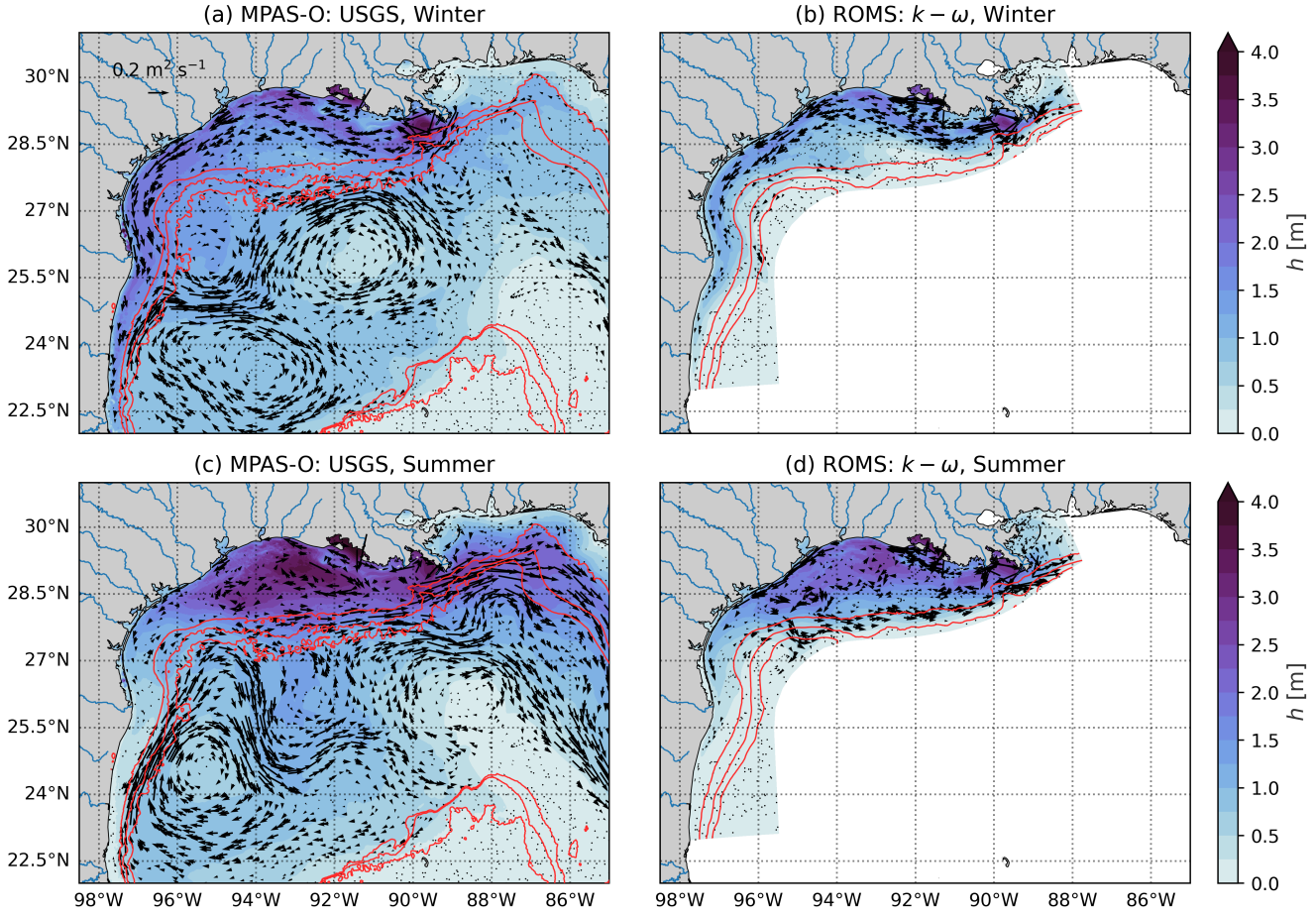


Figure 11. Plan view plots of combined freshwater thickness and flux vectors for the M-A Rivers for MPAS-O: USGS and ROMS: $k-\omega$ during (a-b) winter and (c-d) summer, respectively. The red lines mark the 100, 500, and 1000 m isobaths to emphasize the continental slopes. The ROMS: KPP simulation is similar to ROMS: $k-\omega$ and is not shown.

onto the ROMS grid using Delaunay triangulation. On the Louisiana shelf, ROMS: $k-\omega$ is significantly fresher than MPAS-O: JRA (ΔSSS $<$ -9 g kg^{-1}; Fig. 12e) due to the underestimation of Atchafalaya River discharge. The imprint of MPAS-O: JRA's river spreading is visible in both the SSS (Fig. 12a) and the ΔSSS fields (Fig. 12e). ROMS is saltier north of the Mississippi delta because brackish water from Lake Pontchartrain and the Mobile River is excluded. Qualitatively, ROMS: $k-\omega$ more closely resembles MPAS-O: USGS than JRA on the Louisiana shelf but is saltier almost everywhere. SST is relatively uniform on the shelf in summer (Fig. 12g-j). As a result, the differences between ROMS: $k-\omega$ and both MPAS-O simulations (ΔSST) are approximately ± 1.5°C despite the lack of eddies in MPAS-O (Fig. 12k-l). ROMS: $k-\omega$ is slightly warmer (Δ SST$<$0.5°C) than both MPAS simulations, except close to the river discharge points, likely due to differences in how river temperatures are prescribed (see §2).

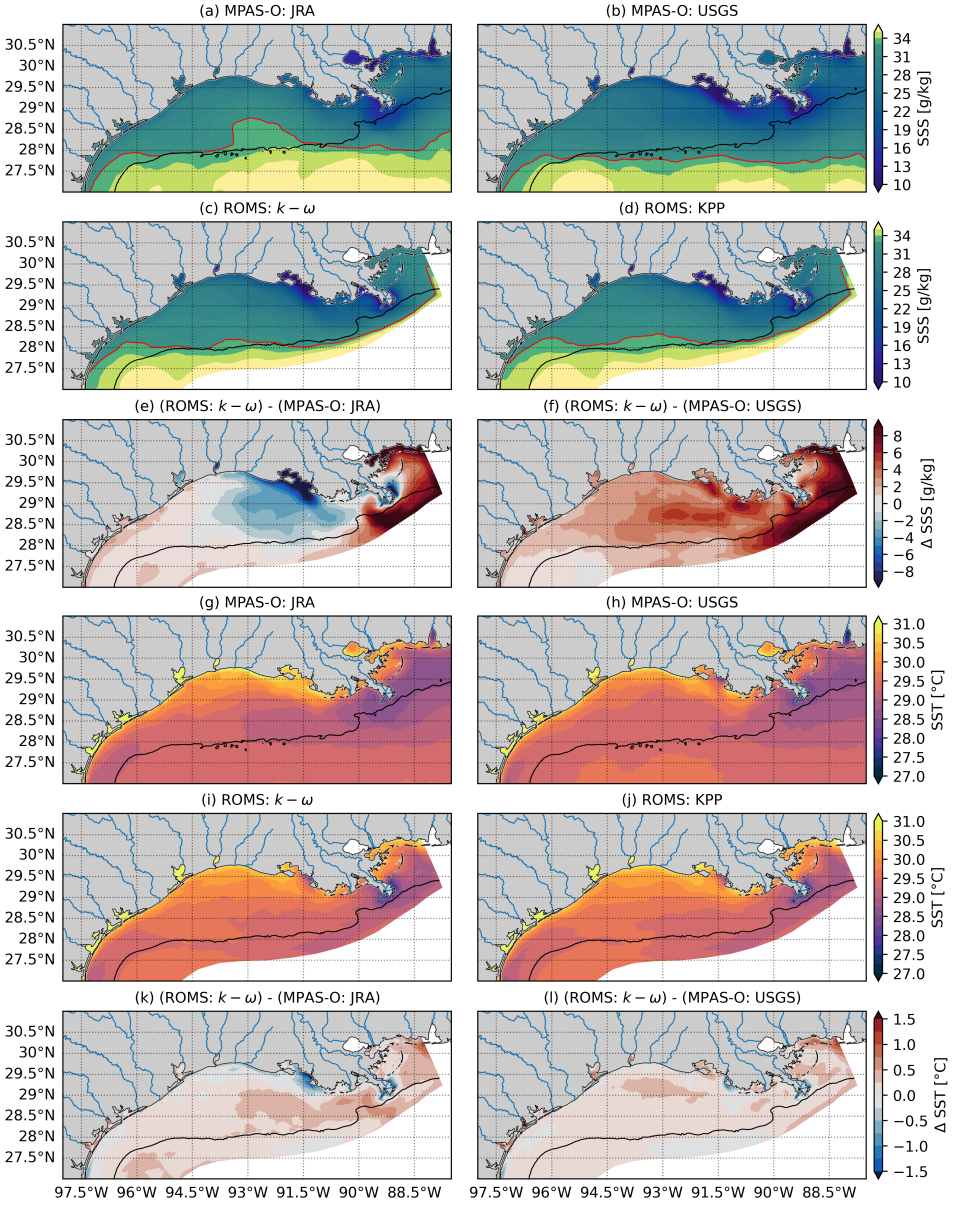


Figure 12. (a-d) Sea surface salinity (SSS) averaged over summer for the 4 simulations. In (a), SSS output from years 3-4 is used. In (b-d), SSS output from years 3-5 is used. The black line marks the 100 m isobath and the red line marks the 33 g kg^{-1} isohaline, the boundary of the M-A plume. Note that SSS plots use a colormap constructed with piecewise linear normalization about SSS=33 g kg^{-1} to emphasize plume versus oceanic water. (e) SSS difference between ROMS: $k-\omega$ and MPAS-O: JRA interpolated onto the ROMS grid. (f) Same as (e), but for the MPAS-O: USGS simulation. (g-l) Same as (a-f), but for sea surface temperature (SST).

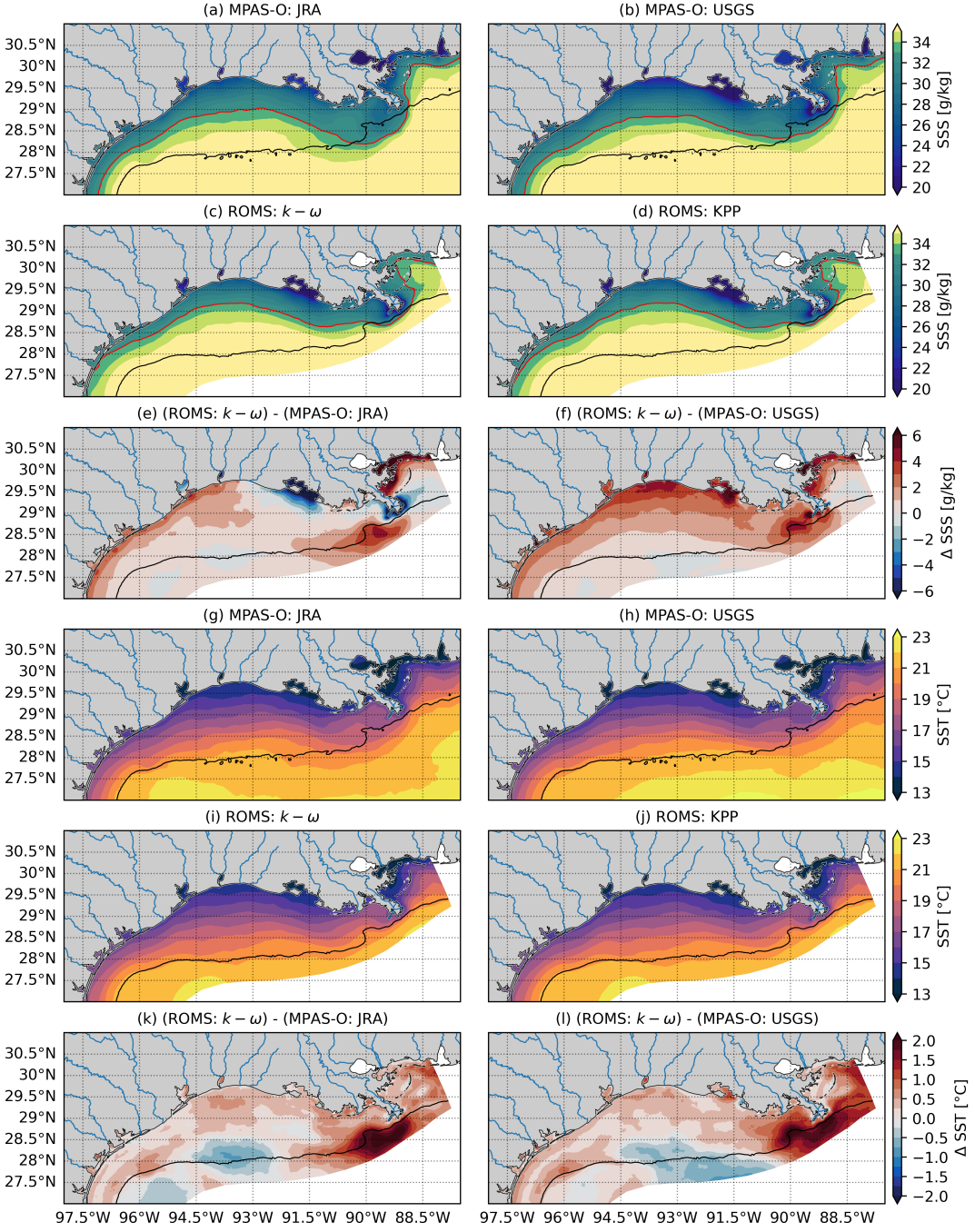


Figure 13. (a-d) Same as Fig. 12, but for winter. Note the difference in colorbar range.

In winter, the salinity fields and plume boundary between MPAS-O and ROMS are more similar. The shelf becomes saltier as the plume is confined closer to the coast (Fig. 13a-d). As a result, ΔSSS shrinks (Fig. 13e-f), with ROMS: $k-\omega$ remaining fresher than MPAS-O: JRA near Atchafalaya Bay (ΔSSS $<$ 6 g kg^{-1}). The opposite is true for MPAS-O: USGS, with it being fresher than ROMS: $k-\omega$ (ΔSSS $<$ -6 g kg^{-1}) near Atchafalaya Bay. As the SST distribution broadens (Fig. 13g-l), ΔSST increases to over 2°C southwest of Bird's Foot for both MPAS-O simulations, but is smaller almost everywhere else. These results suggest MPAS-O demonstrates increased performance in winter when larger eddies are naturally suppressed despite elevated freshwater content from the previous summer influencing the results.

4 Discussion and conclusions

Previous studies with unstructured grid models have shown promise in their ability to seamlessly integrate coastal processes with the global circulation (Mathis et al., 2022; Zhang et al., 2023). However, none have focused on coastal submesoscale dynamics. Here, we have assessed an unstructured global model's ability (MPAS-O) to represent submesoscale dynamics using regional refinement. Encouraged by MPAS-O's performance in idealized simulations in Part I (Hinson et al., 2026), we focused on the Texas–Louisiana (TXLA) shelf in the northern Gulf of Mexico (nGoM). This region is strongly influenced by discharge from the Mississippi and Atchafalaya (M-A) Rivers and regional winds. The defining dynamical feature of this region is a submesoscale eddy field with characteristic diameters of $\mathcal{O}$(20-50 km) that form during summer in response to weakly upcoast winds (Hetland, 2017; Qu et al., 2022). During non-summer months, winds become downcoast and confine the plume closer to the coast, causing submesoscale variability to consist of smaller-scale fronts, filaments, and vortices (Hetland, 2017; Kobashi and Hetland, 2020).

To assess MPAS-O's fidelity, we compared two simulations, MPAS-O: JRA and MPAS-O: USGS, against a validated ROMS model (Kobashi and Hetland, 2020; Zhang et al., 2012b). All simulations used repeat year forcing from 2003-2004 to isolate differences caused by model physics, numerics, and parameterizations. The MPAS-O simulations differed in their treatment of river runoff, vertical resolution, and explicit lateral mixing coefficients. With the exception of the horizontal grid, the configuration for MPAS-O: JRA is more similar to how MPAS-O is configured for coarser-resolution fully-coupled simulations. For example, MPAS-O: JRA uses external mapping files to laterally spread river runoff where the spreading distance is proportional to the magnitude of the river runoff fluxes (Fig. 3b). The source of river runoff fluxes, Japanese Reanalysis (Stewart et al., 2020), underestimates Atchafalaya River discharge by over an order of magnitude (Fig. 4) compared to streamflow observations. In MPAS-O: USGS, rivers are configured as "pseudo point sources" within the ROMS domain such that the locations of the rivers into the ROMS domain are interpolated onto the MPAS grid. Likewise, MPAS-O used the same streamflow data as ROMS within the ROMS model domain and JRA streamflow elsewhere. However, trial simulations (not shown) that used the same vertical grid and explicit lateral mixing parameters as MPAS-O: JRA did not produce a summer eddy field comparable to the ROMS simulations. In an attempt to alleviate this, we used a higher resolution vertical grid with 0.5 m thick layers (half that of MPAS-O: JRA) and tuned the explicit lateral mixing to be as small as possible, yet eddies remained suppressed. As a result, MPAS-O: USGS has excessive freshwater relative to ROMS on the shelf year round, causing significant salinity ($\mathcal{O}$(10 g kg^{-1}))

differences. The plume also extends much further offshore in MPAS-O: USGS in summer relative to the ROMS simulations. We attribute this behavior in ROMS to the climatological nudging to HYCOM at the open boundaries. By the same metrics, MPAS-O's performance is improved during winter when there is less freshwater on the shelf and the characteristic length scale of submesoscale processes decreases. Thus, a primary finding of this study is that MPAS-O needs significant exploration and improvement to operate well in coastal domains.

An unsatisfying result is that the suppression of summer TXLA shelf eddies in MPAS-O likely arises from interacting numerical and parameterization choices whose combined effects are difficult to disentangle. We speculate on likely and unlikely causes because we hope this will be useful for the community and to future studies. We observe that MPAS-O: USGS develops a persistent brackish lens in the upper 5 m of the water column (Fig. 9a,c,e), even in the plume far-field, which is associated with weaker boundary layer vertical viscosity relative to the ROMS base case (ROMS: k–ω). A plausible explanation is that the CVMix implementation of the K-Profile Parameterization (KPP; Van Roekel et al., 2018) requires substantial tuning. It contains numerous adjustable parameters and the behavior can vary substantially across models and within a single model with variable resolution (Li et al., 2019; Van Roekel et al., 2018). A ROMS simulation employing its native KPP implementation (ROMS: KPP) generates shelf eddies comparable to ROMS: k–ω, despite exhibiting stronger viscosity than either ROMS: k–ω or MPAS-O: USGS (Fig. 9).

The idealized simulations in Part I showed that vertical physical mixing (the destruction of vertical salinity variance) in MPAS-O was higher than ROMS. The simulations also suggested that MPAS-O had less numerical mixing (the spurious mixing generated by the discretization of advection) than ROMS when volume-integrated. However, in the idealized model, a vertically uniform lateral salinity gradient is imposed initially and evolves freely through mixed layer instability, with no ongoing buoyancy source. In the realistic simulations, the M-A plume is continuously forced by riverine freshwater input, which maintains spatially heterogeneous surface density gradients that are sharpened by winds. Thus, the contrasting forcing regimes complicate direct attribution of the suppressed eddy activity to physical and numerical mixing differences. A clear direction for future work would be to add river forcing to the idealized model. However, MPAS-O does not have the capability to apply river forcing in idealized domains and adding this capability is beyond the scope of this study.

Neglecting horizontal momentum associated with river runoff might alter the plume structure near freshwater sources. This likely reduces the lateral shear along the plume front, which could indirectly diminish vertical shear and might contribute to reduced mixing. This may explain why MPAS-O remains much fresher close to the river mouths. Yet, the neglect of horizontal momentum should be localized to the plume's near-field and mid-field by definition (Horner-Devine et al., 2015), as mixing by the wind will mix the plume to a specified depth regardless of the initial condition (Fong and Geyer, 2001; Hetland, 2005). In the plume's far-field, particularly in the middle of the Louisiana continental shelf, details of the near-field plume should not contribute to eddy suppression.

Another design choice that deserves consideration is the z^* vertical coordinate, coupled with the lack of bathymetry smoothing relative to ROMS. Previous studies have shown that z-coordinate models represent flow over topography less accurately than terrain-following coordinates, even when partial bottom cells are used (Barron et al., 2006; Petersen et al., 2015; Wise et al., 2022). We think this is unlikely to be an issue on the TXLA shelf for several reasons: (i) the mean bottom slope is very

gentle ($\mathcal{O}(10^{-3})$, Hetland 2017); (ii) the plume is surface-advected in summer, when eddy suppression is most pronounced, limiting its direct interaction with bottom topography; and (iii) we see no evidence of spurious mixing or flow impedance associated with the interaction of vertical layers and the unsmoothed bathymetry. The idealized experiments with sloping bathymetry in Part I also suggest that vertical coordinate choice (at least on the shelf) is unlikely to contribute to eddy suppression, as velocity profiles and volume-averaged kinetic energy were similar between MPAS-O and ROMS.

An additional difference arises from lateral boundary treatment: ROMS uses repeat-year forcing with climatological nudging (only near the boundaries) to a data-assimilative HYCOM configuration, whereas MPAS-O evolves freely. Previous work with the ROMS model (Marta-Almeida et al., 2013) showed that salinity skill near the M-A plume is largely insensitive to the choice of data-assimilative parent model. This, coupled with the circulation on the inner shelf (inshore of 50 m depth) being modulated by wind forcing (Zhang et al., 2012a, 2014), suggests MPAS-O's suppression of shelf eddies is unlikely to result from its freely evolving configuration.

Despite these limitations, MPAS-O: USGS still qualitatively captures the seasonal evolution of the M-A plume. This was demonstrated by tagging the M-A rivers with passive dyes and conducting a freshwater analysis shown in Fig. 10 similar to (Zhang et al., 2012a), which also highlights the strength of using a single regionally refined global mesh. It allows us to study the fate and transport of M-A discharge into the open GoM and possibly the north Atlantic with more simulation time—an analysis not possible with the ROMS model due to its limited domain. The model also shows promise in its ability to represent submesoscale dynamics in the open ocean, but this requires further investigation. However, simulations that use interannual forcing should be performed so that the model can be validated against observations.

In this paper, we identified key challenges in configuring MPAS-O to simulate submesoscale coastal dynamics using regional refinement. Partly based on the results shown here, two-way nesting ROMS within MPAS-O is being evaluated by the DOE as an alternative to seamlessly integrate coastal and global submesoscale dynamics. We recommend that developers of other unstructured global models employ an idealized model hierarchy with increasing complexity to systematically assess model strengths and limitations; such an approach can clarify whether effort is best invested in improving a single modeling system or developing the coupling infrastructure required for nesting. Overall, our results indicate that substantial development is still required before MPAS-O can produce high-fidelity simulations in coastal regions dominated by submesoscale baroclinic instabilities. However, the improved performance on the TXLA shelf during winter suggests that MPAS-O may be better suited for coastal systems where river forcing is less important, such as the Mid-Atlantic Bight.

Code and data availability. The following can be found at https://doi.org/10.5281/zenodo.17903087, which is an archived Zenodo repository (Schlichting et al., 2026): the E3SM branch with the GoM regionally-refined mesh used to produce the MPAS-O simulations, the COAWST branch used to produce the ROMS simulations, the supplementary material, and the model output and code needed to reproduce the figures. All river streamflow data is freely available from USACE (https://www.mvn.usace.army.mil/) and USGS (https://waterdata.usgs.gov/nwis) and also archived in the Zenodo repository. The HYCOM output used to force the ROMS simulations is freely available at https://www.hycom.org/data/glbu0pt08/expt-19pt1.

Author contributions. D.R.S., K.M.S., and M.R.P contributed to the conceptualization, data curation, formal analysis, investigation, methodology, software, validation, visualization, writing the original draft, review & editing. R.D.H. contributed to the conceptualization, funding acquisition, methodology, supervision, review & editing. K.E.H contributed to the methodology, writing the original draft, review & editing. D.E. contributed to the funding acquisition, review & editing.

Competing interests. The authors declare they have no competing interests.

Acknowledgements. All authors were supported by the Study for Exascale Advances in a High-Resolution Ocean Using ROMS Coupled to E3SM project funded through the U.S. Department of Energy, Office of Science and Office of Advanced Scientific Computing Research Scientific Discovery through Advanced Computing program. The authors acknowledge that ChatGPT was used to assist with code cleaning in the Zenodo archive and for grammar editing of the main text. This research used computational resources from the Perlmutter machine of the National Energy Research Scientific Computing Center (NERSC), a U.S. Department of Energy Office of Science User Facility located at Lawrence Berkeley National Laboratory, under Contract No. DE-AC02-05CH11231. Additional simulations and mesh development used resources provided by the Los Alamos National Laboratory Institutional Computing Program, which is supported by the U.S. Department of Energy National Nuclear Security Administration under Contract No. 89233218CNA000001.

References

Balwada, D., Xiao, Q., Smith, S., Abernathey, R., and Gray, A. R.: Vertical fluxes conditioned on vorticity and strain reveal submesoscale ventilation, Journal of Physical Oceanography, 51, 2883–2901, https://doi.org/10.1175/JPO-D-21-0016.1, 2021.

Barkan, R., McWilliams, J. C., Shchepetkin, A. F., Molemaker, M. J., Renault, L., Bracco, A., and Choi, J.: Submesoscale Dynamics in the Northern Gulf of Mexico. Part I: Regional and Seasonal Characterization and the Role of River Outflow, Journal of Physical Oceanography, 47, 2325–2346, https://doi.org/10.1175/jpo-d-17-0035.1, 2017.

Barron, C. N., Kara, A. B., Martin, P. J., Rhodes, R. C., and Smedstad, L. F.: Formulation, implementation and examination of vertical coordinate choices in the Global Navy Coastal Ocean Model (NCOM), Ocean Modelling, 11, 347–375, 2006.

Bianchi, T. S., DiMarco, S. F., Cowan Jr, J., Hetland, R. D., Chapman, P., Day, J., and Allison, M.: The science of hypoxia in the Northern Gulf of Mexico: A review, Science of the Total Environment, 408, 1471–1484, 10.1016/j.scitotenv.2009.11.047, 2010.

Bracco, A., Liu, G., and Sun, D.: Mesoscale-submesoscale interactions in the Gulf of Mexico: From oil dispersion to climate, Chaos, Solitons & Fractals, 119, 63–72, https://doi.org/10.1016/j.chaos.2018.12.012, 2019.

Burchard, H. and Bolding, K.: GETM—A General Estuarine Transport Model: Scientific Documentation, Tech. Rep. EUR 20253 EN, European Commission, 2002.

Burchard, H. and Rennau, H.: Comparative quantification of physically and numerically induced mixing in ocean models, Ocean Modelling, 20, 293–311, https://doi.org/10.1016/j.ocemod.2007.10.003, 2008.

Callies, J., Ferrari, R., Klymak, J. M., and Gula, J.: Seasonality in submesoscale turbulence, Nature communications, 6, 6862, https://doi.org/10.1038/ncomms7862, 2015.

Danabasoglu, G., Lamarque, J.-F., Bacmeister, J., Bailey, D., DuVivier, A., Edwards, J., Emmons, L., Fasullo, J., Garcia, R., Gettelman, A., et al.: The community earth system model version 2 (CESM2), Journal of Advances in Modeling Earth Systems, 12, e2019MS001 916, 2020.

DiMarco, S. F. and Reid, R. O.: Characterization of the principal tidal current constituents on the Texas-Louisiana shelf, Journal of Geophysical Research: Oceans, 103, 3093–3109, https://doi.org/10.1029/97jc03289, 1998.

Engwirda, D.: JIGSAW-GEO (1.0): Locally orthogonal staggered unstructured grid generation for general circulation modelling on the sphere, Geoscientific Model Development, 10, 2117–2140, https://doi.org/10.5194/gmd-10-2117-2017, 2017.

Epke, M., Linardakis, L., Korn, P., and Brüggemann, N.: Overturning of mixed layer eddies in a submesoscale resolving simulation of the North Atlantic, Journal of Physical Oceanography, 2025.

Fong, D. A. and Geyer, W. R.: Response of a river plume during an upwelling favorable wind event, Journal of Geophysical Research: Oceans, 106, 1067–1084, https://doi.org/10.1029/2000JC900134, 2001.

Fox-Kemper, B., Danabasoglu, G., Ferrari, R., Griffies, S., Hallberg, R., Holland, M., Maltrud, M., Peacock, S., and Samuels, B.: Parameterization of mixed layer eddies. III: Implementation and impact in global ocean climate simulations, Ocean Modelling, 39, 61–78, https://doi.org/10.1016/j.ocemod.2010.09.002, 2011.

Gent, P. R. and McWilliams, J. C.: Isopycnal mixing in ocean circulation models, Journal of Physical Oceanography, 20, 150–155, 1990.

Golaz, J.-C., Lin, W., Zheng, X., Xie, S., Roberts, A., Roekel, L. P. V., Thornton, P. E., Barthel, A., Bradley, A., Wolfe, J. D., et al.: The Energy Exascale Earth System Model version 3. Part II: Overview of the coupled system, ESS Open Archive eprints, 446, essoar–175097 464, 2025.

Große, F., Fennel, K., and Laurent, A.: Quantifying the relative importance of riverine and open-ocean nitrogen sources for hypoxia formation in the northern Gulf of Mexico, Journal of Geophysical Research: Oceans, 124, 5451–5467, https://doi.org/10.1029/2019JC015230, 2019.

Hetland, R. and Hsu, T.: Freshwater and sediment dispersal in large river plumes, Biogeochemical dynamics at large river-coastal interfaces: Linkages with global climate change, pp. 55–85, https://doi.org/10.1017/CBO9781139136853, 2013.

Hetland, R. D.: Relating river plume structure to vertical mixing, Journal of Physical Oceanography, 35, 1667–1688, https://doi.org/10.1175/jpo2774.1, 2005.

Hetland, R. D.: Suppression of baroclinic instabilities in buoyancy-driven flow over sloping bathymetry, Journal of Physical Oceanography, 47, 49–68, https://doi.org/10.1175/jpo-d-15-0240.1, 2017.

Hetland, R. D. and DiMarco, S. F.: Skill assessment of a hydrodynamic model of circulation over the Texas–Louisiana continental shelf, Ocean Modelling, 43, 64–76, https://doi.org/10.1016/j.ocemod.2011.11.009, 2012.

Higdon, R. L.: A two-level time-stepping method for layered ocean circulation models: further development and testing, Journal of Computational Physics, 206, 463–504, https://doi.org/10.1016/j.jcp.2004.12.011, 2005.

Hinson, K., Schlichting, D., Hetland, R. D., Engwirda, D., Smith, K. M., and Uyeda, K.: Towards High-Fidelity Simulations of Coastal Submesoscale Baroclinic Instabilities with MPAS-O Part I: Idealized Experiments, Geoscientific Model Development, 2026.

Hoch, K. E., Petersen, M. R., Brus, S. R., Engwirda, D., Roberts, A. F., Rosa, K. L., and Wolfram, P. J.: MPAS-Ocean simulation quality for variable-resolution North American coastal meshes, Journal of Advances in Modeling Earth Systems, 12, e2019MS001 848, https://doi.org/10.1029/2019MS001848, 2020.

Horner-Devine, A. R., Hetland, R. D., and MacDonald, D. G.: Mixing and transport in coastal river plumes, Annual Review of Fluid Mechanics, 47, 569–594, https://doi.org/10.1146/annurev-fluid-010313-141408, 2015.

Jerlov, N. G.: Optical studies of ocean water, Rept. Swedish Deep-Sea Exped., 3, 1–59, 1951.

Kobashi, D. and Hetland, R.: Reproducibility and variability of submesoscale frontal eddies on a broad, low-energy shelf of freshwater influence, Ocean Dynamics, 70, 1377–1395, https://doi.org/10.1007/s10236-020-01401-4, 2020.

Körner, M., Cusack, J. M., Nash, J., Shearman, R. K., Thomas, L. N., MacKinnon, J., Hsu, F. H. W., Taylor, J., Liu, J., and Hilditch, J. P.: Symmetric instability drives exchange between surface and bottom waters in a coastal front, Science Advances, 12, eaeb9841, 2026.

Large, W. G., McWilliams, J. C., and Doney, S. C.: Oceanic vertical mixing: A review and a model with a nonlocal boundary layer parameterization, Reviews of geophysics, 32, 363–403, https://doi.org/10.1029/94RG01872, 1994.

Lévy, M., Franks, P. J., and Smith, K. S.: The role of submesoscale currents in structuring marine ecosystems, Nature communications, 9, 4758, 2018.

Li, Q., Reichl, B. G., Fox-Kemper, B., Adcroft, A. J., Belcher, S. E., Danabasoglu, G., Grant, A. L., Griffies, S. M., Hallberg, R., Hara, T., et al.: Comparing ocean surface boundary vertical mixing schemes including Langmuir turbulence, Journal of Advances in Modeling Earth Systems, 11, 3545–3592, https://doi.org/10.1029/2019MS001810, 2019.

Liu, G., Bracco, A., and Sitar, A.: Submesoscale mixing across the mixed layer in the Gulf of Mexico, Frontiers in Marine Science, 8, 615 066, https://doi.org/10.3389/fmars.2021.615066, 2021.

Marta-Almeida, M., Hetland, R. D., and Zhang, X.: Evaluation of model nesting performance on the Texas-Louisiana continental shelf, Journal of Geophysical Research: Oceans, 118, 2476–2491, https://doi.org/10.1002/jgrc.20163, 2013.

Mathis, M., Logemann, K., Maerz, J., Lacroix, F., Hagemann, S., Chegini, F., Ramme, L., Ilyina, T., Korn, P., and Schrum, C.: Seamless integration of the coastal ocean in global marine carbon cycle modeling, Journal of Advances in Modeling Earth Systems, 14, e2021MS002 789, https://doi.org/10.1029/2021MS002789, 2022.

McWilliams, J. C.: Submesoscale currents in the ocean, Proceedings of the Royal Society A: Mathematical, Physical and Engineering Sciences, 472, 20160 117, https://doi.org/10.1098/rspa.2016.0117, 2016.

McWilliams, J. C., Huckle, E., and Shchepetkin, A. F.: Buoyancy effects in a stratified Ekman layer, Journal of Physical Oceanography, 39, 2581–2599, https://doi.org/10.1175/2009JPO4130.1, 2009.

Ntaganou, N., Chassignet, E. P., and Bozec, A.: Impact of horizontal model resolution on mixing and dispersion in the northeastern Gulf of Mexico, Journal of Geophysical Research: Oceans, 129, e2024JC021 315, https://doi.org/10.1029/2024JC021315, 2024.

Paulson, C. A. and Simpson, J. J.: Irradiance measurements in the upper ocean, Journal of Physical Oceanography, 7, 952–956, 1977.

Petersen, M. R., Jacobsen, D. W., Ringler, T. D., Hecht, M. W., and Maltrud, M. E.: Evaluation of the arbitrary Lagrangian–Eulerian vertical coordinate method in the MPAS-Ocean model, Ocean Modelling, 86, 93–113, https://doi.org/10.1016/j.ocemod.2014.12.004, 2015.

Petersen, M. R., Asay-Davis, X. S., Berres, A. S., Chen, Q., Feige, N., Hoffman, M. J., Jacobsen, D. W., Jones, P. W., Maltrud, M. E., Price, S. F., et al.: An evaluation of the ocean and sea ice climate of E3SM using MPAS and interannual CORE-II forcing, Journal of Advances in Modeling Earth Systems, 11, 1438–1458, https://doi.org/10.1029/2018MS001373, 2019.

Qu, L., Thomas, L. N., and Hetland, R. D.: Near-inertial-wave critical layers over sloping bathymetry, Journal of Physical Oceanography, 51, 1737–1756, https://doi.org/10.1175/jpo-d-20-0221.1, 2021.

Qu, L., Thomas, L. N., Wienkers, A. F., Hetland, R. D., Kobashi, D., Taylor, J. R., Hsu, F. H. W., MacKinnon, J. A., Shearman, R. K., and Nash, J. D.: Rapid vertical exchange at fronts in the Northern Gulf of Mexico, Nature communications, 13, 1–11, https://doi.org/10.1038/s41467-022-33251-7, 2022.

Redi, M. H.: Oceanic isopycnal mixing by coordinate rotation, Journal of Physical Oceanography, 12, 1154–1158, https://doi.org/10.1175/1520-0485(1982)012<1154:OIMBCR>2.0.CO;2, 1982.

Ringler, T., Petersen, M., Higdon, R. L., Jacobsen, D., Jones, P. W., and Maltrud, M.: A multi-resolution approach to global ocean modeling, Ocean Modelling, 69, 211–232, https://doi.org/10.1016/j.ocemod.2013.04.010, 2013.

Ringler, T. D., Thuburn, J., Klemp, J. B., and Skamarock, W. C.: A unified approach to energy conservation and potential vorticity dynamics for arbitrarily-structured C-grids, Journal of Computational Physics, 229, 3065–3090, https://doi.org/doi.org/10.1029/2019MS001954, 2010.

Roobaert, A., Laruelle, G. G., Landschützer, P., Gruber, N., Chou, L., and Regnier, P.: The spatiotemporal dynamics of the sources and sinks of CO2 in the global coastal ocean, Global Biogeochemical Cycles, 33, 1693–1714, 2019.

Savelli, R., Carroll, D., Menemenlis, D., Lauderdale, J. M., Bertin, C., Dutkiewicz, S., Manizza, M., Bloom, A. A., Castro-Morales, K., Miller, C. E., et al.: Implementing riverine biogeochemical inputs in ECCO-Darwin: a sensitivity analysis of terrestrial fluxes in a data-assimilative global ocean biogeochemistry model, Geoscientific Model Development, 19, 867–885, 2026.

Schlichting, D., Qu, L., Kobashi, D., and Hetland, R.: Quantification of physical and numerical mixing in a coastal ocean model using salinity variance budgets, Journal of Advances in Modeling Earth Systems, 15, e2022MS003 380, https://doi.org/10.1029/2022MS003380, 2023.

Schlichting, D., Hetland, R. D., and Jones, C. S.: Numerical mixing suppresses submesoscale baroclinic instabilities over sloping bathymetry, Journal of Advances in Modeling Earth Systems, https://doi.org/10.1029/2024MS004321, 2024.

Schlichting, D., Smith, K., Petersen, M., Hetland, R., Hinson, K., and Engwirda, D.: Towards high-fidelity simulations of Coastal Submesoscale Baroclinic Instabilities with MPAS-O Part II: Data and Code, Dataset, https://doi.org/10.5281/zenodo.17903087, 2026.

Shchepetkin, A. F. and McWilliams, J. C.: Quasi-monotone advection schemes based on explicit locally adaptive dissipation, Monthly weather review, 126, 1541–1580, https://doi.org/10.1175/1520-0493(1998)126<1541:QMASBO>2.0.CO;2, 1998.

Shchepetkin, A. F. and McWilliams, J. C.: The Regional Oceanic Modeling System (ROMS): A split-explicit, free-surface, topography-following-coordinate oceanic model, Ocean modelling, 9, 347–404, https://doi.org/10.1016/j.ocemod.2004.08.002, 2005.

Shchepetkin, A. F. and McWilliams, J. C.: Computational kernel algorithms for fine-scale, multiprocess, longtime oceanic simulations, in: Handbook of numerical analysis, vol. 14, pp. 121–183, Elsevier, 2009.

Shcherbina, A. Y., D'Asaro, E. A., Lee, C. M., Klymak, J. M., Molemaker, M. J., and McWilliams, J. C.: Statistics of vertical vorticity, divergence, and strain in a developed submesoscale turbulence field, Geophysical Research Letters, 40, 4706–4711, https://doi.org/10.1002/grl.50919, 2013.

Skamarock, W. C. and Gassmann, A.: Conservative transport schemes for spherical geodesic grids: High-order flux operators for ODE-based time integration, Monthly Weather Review, 139, 2962–2975, https://doi.org/10.1175/MWR-D-10-05056.1, 2011.

Smith, K. M., Hamlington, P. E., and Fox-Kemper, B.: Effects of submesoscale turbulence on ocean tracers, Journal of Geophysical Research: Oceans, 121, 908–933, https://doi.org/https://doi.org/10.1002/2015JC011089, 2016.

Smolarkiewicz, P. K. and Margolin, L. G.: MPDATA: A finite-difference solver for geophysical flows, Journal of Computational Physics, 140, 459–480, https://doi.org/10.1006/jcph.1998.5901, 1998.

Sorourian, S., Huang, H., Xu, K., Justic, D., and D'Sa, E. J.: A modeling study of water and sediment flux partitioning through the major passes of Mississippi Birdfoot Delta and their plume structures, Geomorphology, 401, 108 109, https://doi.org/10.1016/j.geomorph.2022.108109, 2022.

Stefan, H. G. and Preud'homme, E. B.: Stream temperature estimation from air temperature 1, Journal of the American Water Resources Association, 29, 27–45, https://doi.org/10.1111/j.1752-1688.1993.tb01502.x, 1993.

Stewart, K., Kim, W., Urakawa, S., Hogg, A., Yeager, S., Tsujino, H., Nakano, H., Kiss, A., and Danabasoglu, G.: JRA55-do-based repeat year forcing datasets for driving ocean–sea-ice models, Ocean Modelling, 147, 101 557, https://doi.org/10.1016/j.ocemod.2019.101557, 2020.

Sun, Q., Whitney, M. M., Bryan, F. O., and Tseng, Y.-h.: A box model for representing estuarine physical processes in Earth system models, Ocean Modelling, 112, 139–153, 2017.

Suzuki, T., Yamazaki, D., Tsujino, H., Komuro, Y., Nakano, H., and Urakawa, S.: A dataset of continental river discharge based on JRA-55 for use in a global ocean circulation model, Journal of Oceanography, 74, 421–429, https://doi.org/10.1007/s10872-017-0458-5, 2018.

Tang, Q., Golaz, J.-C., Van Roekel, L. P., Taylor, M. A., Lin, W., Hillman, B. R., Ullrich, P. A., Bradley, A. M., Guba, O., Wolfe, J. D., et al.: The fully coupled regionally refined model of E3SM version 2: overview of the atmosphere, land, and river results, Geoscientific Model Development, 16, 3953–3995, https://doi.org/10.5194/gmd-16-3953-2023, 2023.

Taylor, J. R. and Thompson, A. F.: Submesoscale dynamics in the upper ocean, Annual Review of Fluid Mechanics, 55, 103–127, https://doi.org/10.1146/annurev-fluid-031422-095147, 2023.

Thyng, K. M. and Hetland, R. D.: Seasonal and interannual cross-shelf transport over the Texas and Louisiana continental shelf, Continental Shelf Research, 160, 23–35, https://doi.org/10.1016/j.csr.2018.03.006, 2018.

Turner, A. K., Lipscomb, W. H., Hunke, E. C., Jeffery, N., Engwirda, D., Ringler, T. D., Wolfe, J. D., et al.: MPAS-Seaice (v1. 0.0): sea-ice dynamics on unstructured Voronoi meshes, Geoscientific Model Development, 15, 3721–3751, https://doi.org/10.5194/gmd-15-3721-2022, 2022.

Uchida, T., Le Sommer, J., Stern, C., Abernathey, R., Holdgraf, C., Albert, A., Brodeau, L., Chassignet, E., Xu, X., Gula, J., et al.: Cloud-based framework for inter-comparing submesoscale permitting realistic ocean models, Geoscientific Model Development Discussions, 2022, 1–32, 2022.

Van Roekel, L., Adcroft, A. J., Danabasoglu, G., Griffies, S. M., Kauffman, B., Large, W., Levy, M., Reichl, B. G., Ringler, T., and Schmidt, M.: The KPP boundary layer scheme for the ocean: Revisiting its formulation and benchmarking one-dimensional simulations relative to LES, Journal of Advances in Modeling Earth Systems, 10, 2647–2685, https://doi.org/10.1029/2018MS001336, 2018.

Warner, J. C., Sherwood, C. R., Arango, H. G., and Signell, R. P.: Performance of four turbulence closure models implemented using a generic length scale method, Ocean Modelling, 8, 81–113, https://doi.org/10.1016/j.ocemod.2003.12.003, 2005.

Wise, A., Harle, J., Bruciaferri, D., O'Dea, E., and Polton, J.: The effect of vertical coordinates on the accuracy of a shelf sea model, Ocean Modelling, 170, 101 935, 2022.

Wiseman, W. J., Rabalais, N., Turner, R., Dinnel, S., and MacNaughton, A.: Seasonal and interannual variability within the Louisiana coastal current: stratification and hypoxia, Journal of Marine Systems, 12, 237–248, https://doi.org/10.1016/S0924-7963(96)00100-5, 1997.

Zhang, W. and Hetland, R. D.: A study of baroclinic instability induced convergence near the bottom using water age simulations, Journal of Geophysical Research: Oceans, 123, 1962–1977, https://doi.org/10.1002/2017JC013561, 2018.

Zhang, X., Hetland, R. D., Marta-Almeida, M., and DiMarco, S. F.: A numerical investigation of the Mississippi and Atchafalaya freshwater transport, filling and flushing times on the Texas-Louisiana Shelf, Journal of Geophysical Research: Oceans, 117, https://doi.org/10.1029/2012jc008108, 2012a.

Zhang, X., Marta-Almeida, M., and Hetland, R. D.: A high-resolution pre-operational forecast model of circulation on the Texas-Louisiana continental shelf and slope, Journal of Operational Oceanography, 5, 19–34, https://doi.org/10.1080/1755876X.2012.11020129, 2012b.

Zhang, Y. J., Fernandez-Montblanc, T., Pringle, W., Yu, H.-C., Cui, L., and Moghimi, S.: Global seamless tidal simulation using a 3D unstructured-grid model (SCHISM v5. 10.0), Geoscientific Model Development, 16, 2565–2581, https://doi.org/10.5194/gmd-16-2565-2023, 2023.

Zhang, Z., Hetland, R., and Zhang, X.: Wind-modulated buoyancy circulation over the Texas-Louisiana shelf, Journal of Geophysical Research: Oceans, 119, 5705–5723, https://doi.org/10.1002/2013JC009763, 2014.